

Article

Agate Mineralization in Paleoproterozoic Organic Carbon-Rich Sedimentary Rocks of the Onega Basin (NW Russia): Insights into Genesis

Evgeniya N. Svetova , Sergei A. Svetov and Oleg B. LavrovInstitute of Geology, Karelian Research Centre of RAS, 185910 Petrozavodsk, Russia;
ssvetov@krc.karelia.ru (S.A.S.); lavrkokolok1802@yandex.ru (O.B.L.)

* Correspondence: enkotova@rambler.ru

Abstract: In this contribution, we present the results of mineralogical investigation of the agates in Paleoproterozoic organic carbon-rich sedimentary rocks within the Onega Basin (Fennoscandian shield, Russia) aimed at reconstructing the agate-forming processes. Optical and scanning electron microscopy, EDS microanalysis, thermal analysis, X-ray powder diffraction, Raman spectroscopy, and carbon isotope analysis were used for the study. Three main varieties of agates differing in morphology and texture were identified, including concentrically zoned nodules, fine-banded, and carbon-rich moss agates. Mineralogical evidence indicates the participation of hydrothermal fluids in agate formation. Concentrically zoned nodules could be formed due to the dissolution of carbonate concretions in the organic carbon-rich siltstones and their silicification as a result of late hydrothermal processes. Fine-banded vein agates occur in stockworks crosscutting organic carbon-rich rocks and are widely accompanied by sulfides, selenides, carbonates, sulfates, and iron oxides. Carbonaceous matter in moss agates is present as poorly ordered carbon and is characterized by a low $\delta^{13}\text{C}_{\text{org}}$ value (-25.64%), suggesting a biogenic origin. Raman spectroscopy data showed an elevated amount of moganite besides alpha quartz in the concentrically zoned nodules compared to other agate varieties, indicating different ages of the mineralization processes. We suggest that the revealed varieties of agates were formed at different stages of long-term hydrothermal processes occurring in the Onega Basin.

Keywords: agate; Paleoproterozoic; organic carbon-rich rocks; Fennoscandian Shield; Onega Basin; X-ray diffraction; Raman spectroscopy; SEM-EDS; carbonaceous matter



Citation: Svetova, E.N.; Svetov, S.A.; Lavrov, O.B. Agate Mineralization in Paleoproterozoic Organic Carbon-Rich Sedimentary Rocks of the Onega Basin (NW Russia): Insights into Genesis. *Minerals* **2024**, *14*, 447. <https://doi.org/10.3390/min14050447>

Academic Editors: Magdalena Dumańska-Słowik, Jens Götze and Tomasz Powolny

Received: 28 February 2024

Revised: 19 April 2024

Accepted: 22 April 2024

Published: 24 April 2024



Copyright: © 2024 by the authors. Licensee MDPI, Basel, Switzerland. This article is an open access article distributed under the terms and conditions of the Creative Commons Attribution (CC BY) license (<https://creativecommons.org/licenses/by/4.0/>).

1. Introduction

The Paleoproterozoic Onega Basin represents one of the largest fragments of continental margin preserved on the eastern part of the Fennoscandian Shield [1]. It consists of well-preserved low metamorphic-grade volcano-sedimentary succession aged 2500–1700 Ma and is of high interest as a unique archive of the geological evolution of the Earth, the sedimentation and volcanic processes, the composition of the hydrosphere and atmosphere of the Earth, and the evolution of early life [1–4].

The Onega Basin is famous worldwide for its carbonate, high carbon-rich rocks (named “shungites” after Inostrantsev, 1879 [5]), as well as the oldest evaporites in the world, marking a global change in geodynamic regimes of the Earth [1,3,4,6,7].

The Onega Basin area is characterized by ore deposits of varying scale and genesis. Burakovka layered intrusions belongs to the most important chromite deposits in Europe and contain considerable amounts of platinum group elements [8,9]. Of note are titanomagnetite deposits associated with Pudozhgora and Koykary-Svyatnavolok intrusions [10], as well as Cu-(Au-Pd-Pt-Mo)-U-V deposits of hydrothermal-metasomatic genesis, confined to mafic, carbonate, and carbon-rich rocks [11,12].

The hydrothermal activity in the Onega Basin led to the appearance of agate mineralization in the volcanic complexes of the Ludicovian super-horizon (2100–1920 Ma) [13,14]. Agates occur mostly as an infill of fissures, cavities, and gas vesicles in pillow and massive lavas. They display diversity in morphology and microtextural features. Besides the abundant lightly colored agates, extremely rare “black agates” containing carbonaceous matter disseminated in the silica matrix can be found. The previous study of agates assumed that agate formation was related to the Svecofenian orogeny within 1980–1750 Ma [13,14].

Agate mineralization also occurs locally in the sedimentary rocks of the LSH within the Onega Basin. Due to the scarcity of data on mineralogy and formation conditions, an agate occurrence located on the northeast coast of Velikaya Guba Bay of Lake Onega in the organic carbon-rich sedimentary rocks was the focus of the present study. The results of investigations of agate-bearing rock, agates, and accompanied mineralized veins provide new data for the reconstruction of agate-forming processes in the Paleoproterozoic sedimentary rocks within the Onega Basin.

2. Geological Setting

The Onega Basin is located in the southeastern part of the Archean Karelian Craton in the Fennoscandian Shield [1]. It contains a well-studied Paleoproterozoic (2.5–1.7 Ga) volcano-sedimentary sequence that rests unconformably on an Archean granite-greenstone and tonalite-trondhjemite-granodiorite association [1,15–18].

The volcano-sedimentary sequence is subdivided into six super-horizons: Sumian (2.5–2.4 Ga), Sariolian (2.4–2.3 Ga), Yatulian (2.3–2.1 Ga), Ludicovian (2.1–1.9 Ga), Kalevian (1.92–1.8 Ga), and Vepsian (1.8–1.7 Ga).

The Ludicovian super-horizon (LSH) includes the lower Zaonega Formation and the upper Suisari Formation (Figure 1) [1,19].

The Zaonega Formation (ZF) varies in thickness from 1100 to 1800 m and has the greatest areal distribution compared to other formations in the Onega Basin. The ZF is subdivided into two subformations: a lower carbonate-argillite sequence (100–200 m) comprising interbedded sandstones, siltstones, mudstones (containing organic carbon up to 3%), and carbonates; and an upper volcano-sedimentary sequence (800–900 m) [6,20–22]. Sedimentary rocks of the upper sequences include siltstones and sandstones with high organic carbon content up to 80 wt.%. Numerous studies have shown that carbon matter in the ZF sedimentary rocks is biogenic in origin and forms a giant Paleoproterozoic oilfield known as “Shunga” [1,4,6,23–26]. The organic carbon-rich rocks yield an Re–Os isochron with an age of ca. 2050 Ma [27] and have low $\delta^{13}\text{C}_{\text{org}}$ values, from -17 to -46‰ [4,24,25]. Volcanic rocks include plagiophyric massive and pillow andesite basalts, tuffs, and tuffites. The age of the ZF is estimated at 2100–1980 Ma [1,2,16,28,29]. Our focus is agates found in the sedimentary rocks confined to the base of the upper subformation of the ZF (Figure 1).

The Suisari Formation (SF) varies in thickness from 300 to 1000 m and comprises picrite-picobasaltic lavas interbedded with tuffs and tuffites [1,30]. It is separated from the ZF by a horizon of polymictic conglomerates and gritstones, overlying the ZF with angular unconformity. A depositional age of the SF according to Sm/Nd isotopic data is 1980–1950 Ma [2,30].

The magmatic complex of LSH comprises dykes and gabbro-dolerite sills. The U–Pb zircon age of quartz dolerites from the eastern part of the Zaonega Peninsula is 1956 ± 5 Ma [28], the Konchozero gabbro-dolerite sill is 1975 ± 24 Ma [2], and the Pazha gabbro-dolerite sill is 1961.6 ± 5.1 Ma [29].

The volcanic and sedimentary rocks of the LSH were deformed and metamorphosed during the Svecofenian orogeny (ca. 1780–1750 Ma) [31]. The P–T conditions (1–3 kbar, 290–320 °C) of the metamorphism achieved prehnite-pumpellyite facies [32].

The intrusion of gabbro-dolerite sills (1980–1950 Ma) is responsible for the earliest interval of hydrothermal alteration of the LSH (mainly in the ZF) rocks [27–29]. The sills triggered hydrothermal fluid flow and redistribution of carbonaceous material associated with epigenetic sulfide mineralization [33]. Several subsequent peaks of hydrothermal

activity at 1780–1500 Ma were recognized in the southwestern part of the Onega Basin using Rb-Sr isotope study of altered rocks [34].

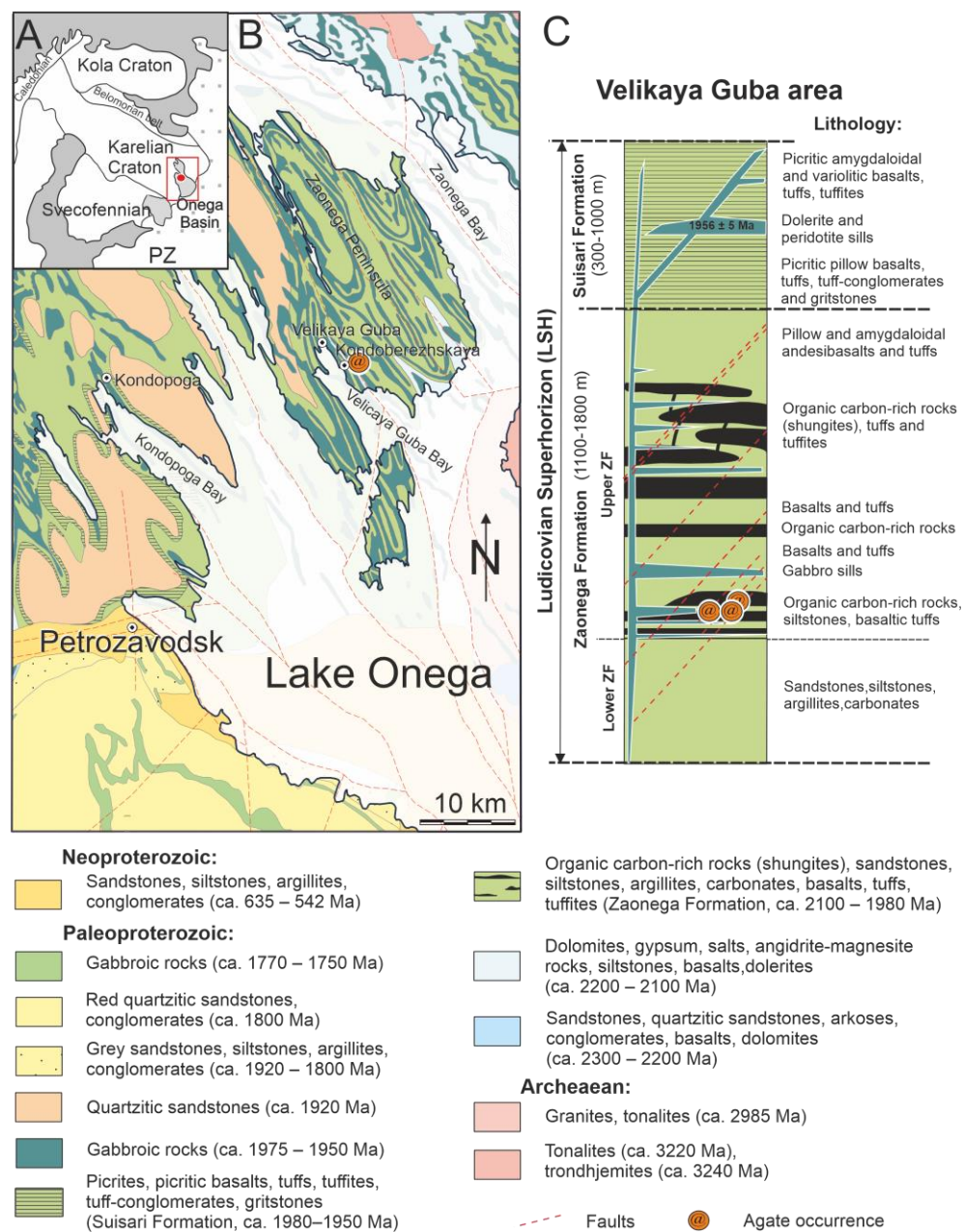


Figure 1. (A) Position of studied area. (B) Simplified geological map of the northwestern part of the Onega Basin based on [16]. (C) Simplified geological section of the Ludicovian super-horizon based on [1]. The stratigraphic positions of studied samples are shown by red @-symbols.

3. Agate Occurrence

The studied area is located near the Kondoberezhskaya village on the northeast coast of the Velikaya Guba Bay of Lake Onega (Figure 1B). Along the shoreline, bedrocks are overlain by Quaternary deposits, including post-glacial clastic material of short-range transport [35]. In the 1980s, an occurrence of variegated jasper and agates was discovered here as a result of geologic exploration carried out by the “Severquartzsamotzvetvy” company [35]. Agates occur within the organic-rich sedimentary rocks as spectacular spherical nodules and display banding of mostly reddish, orange, and white colors (Figure 2). The thickness of the moraine cover in the study area, according to drilling data, varies from 2 to 10 m.

Sedimentary bedrocks with agate nodules are mainly exposed in small mine workings. The rocks are cut by numerous quartz veins forming stockworks. Fine-banded agates reddish in color were also recognized within such veins and veinlets (Figure 3A,B,D). Locally, fissures and cavities are filled by quartz-chalcedony aggregates smoky-black in color (Figure 3C).

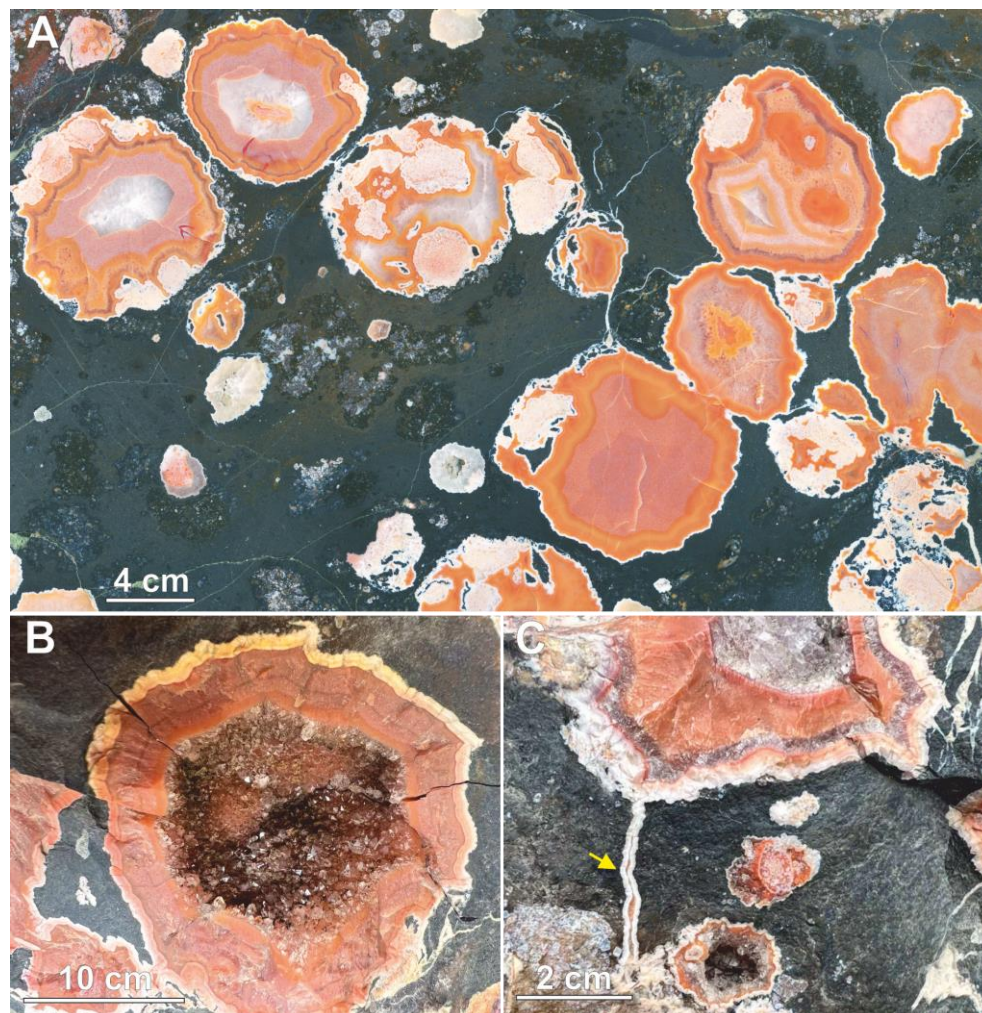


Figure 2. Photographs of concentrically zoned agates in the Paleoproterozoic organic carbon-rich sedimentary rocks within the Onega Basin LSH (ZF) (exhibition sample from the museum of the IG KRC RAS). (A) Image of polished slab of agate-bearing rocks illustrating diversified textures in agates; (B) image showing rough-banded agate with central cavity covered by amethyst-like crystals; (C) image displaying channel of Fe-bearing solution migration (marked by yellow arrow).

Gemstone material (sedimentary rock debris with agates) is mainly concentrated in the upper layer of the moraine at a depth of 0.3–1 m. Agates are characterized by high decorative properties and can be of interest as collectible and ornamental stones. However, it is very difficult to estimate the scale of agate mineralization and the gemological potential of the studied area due to the limited bedrock exposure.

During field work, we examined an old quarry that has been preserved after geological exploration. Fragments of host rocks with agate mineralization were found within the clastic material.

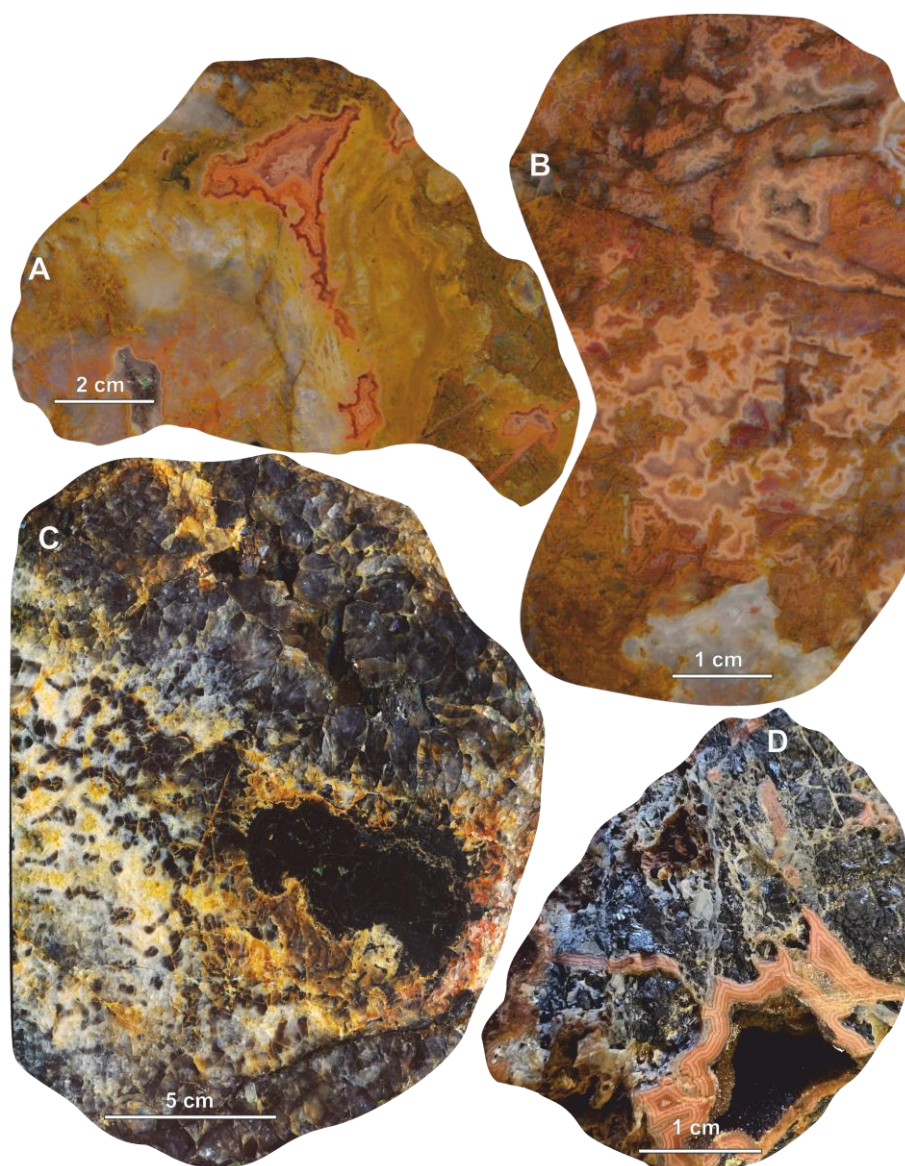


Figure 3. Photographs of agates from veins in the organic carbon-rich sedimentary rocks within the Onega Basin LSH (ZF). Fine-banded (A,B) agates with Fe-oxide/hydroxide pigment disseminated along individual chalcedony layers; (C) moss agate enriched in carbon and Fe-oxides. A smoky quartz druse is visible in the top right corner; (D) fine-banded Fe-oxide-rich agate within the vein stockwork sample composed of quartz, sphalerite, chalcopyrite, and native sulfur.

4. Materials and Methods

Agates, mineralized quartz veins, and parent organic carbon-rich host rocks were examined using optical microscopy, scanning electron microscopy with energy-dispersive spectroscopy (SEM-EDS), powder X-ray diffraction (XRD), thermal analysis, Raman spectroscopy, and wet chemistry at the Institute of Geology, Karelian Research Centre, Russian Academy of Sciences (IG KRC RAS, Petrozavodsk, Russia).

Three representative agate samples of different texture and color, and four samples of ore-bearing quartz veins, as well as parent organic carbon-rich rock samples, were selected for detailed mineralogical investigation.

The agate thin sections were examined using transmitted light microscopy on a Polam-211 polarization microscope. SEM-EDS investigation was performed on carbon-coated polished sections using a VEGA II LSH (Tescan, Brno, Czech Republic) scanning electron microscope with EDS INCA Energy 350 (Oxford Instruments, Oxford, UK). The analyses

were carried out under the following operation condition: W cathode, 20 kV accelerating voltage, 20 mA beam current, 2 μm beam diameter, and 90 s counting time. A set of standards of rock-forming minerals was used. SEM-EDS quantitative data and determination of the analysis accuracy were acquired and processed using the Microanalysis Suite Issue 12, INCA Suite v. 4.01.

Major element contents in the agates and host rock samples were determined by wet chemistry.

Thermal properties of the organic carbon-rich rock were determined on a NETZSCH STA 449 F1 Jupiter (Selb, Germany) thermoanalyzer. For this experiment, 10 mg of powdered sample was placed into a platinum-rhodium crucible and heated from room temperature to 1200 $^{\circ}\text{C}$ in an air atmosphere with a rate of 10 $^{\circ}\text{C}/\text{min}$.

Powder XRD was applied to determine mineral composition of agates and host rock samples, and to analyze structural parameters of quartz. It was conducted using a Thermo Scientific ARL X'TRA diffractometer (Thermo Fisher Scientific, Ecublens, Switzerland) with Cu-K α radiation (voltage 40 kV, current 30 mA). Diffractograms were recorded over the 2θ angular range of 5 to 75 $^{\circ}$ 2θ with a scanning step of 0.4 $^{\circ}$ $2\theta/\text{min}$. Diffractograms of agate samples in the 25–28 $^{\circ}$ and 66–69 $^{\circ}$ 2θ ranges were collected with a scanning step of 0.2 $^{\circ}$ $2\theta/\text{min}$ for more precise estimation of quartz parameters. Phase analysis was performed using Win XRD software v.2.0-6 and the ICDD database. A quantitative determination of the relative contents of mineral phases was realized by the Rietveld method with Siroquant v.3.0 software. The samples were hand-ground to achieve grain sizes < 50 μm . The detection limit for XRD phase identification was 3 wt.%.

Raman spectroscopy was applied to characterize SiO₂ polymorphs and Fe-oxides/hydroxide phases in agates, as well as to analyze structural characteristics of the carbonaceous matter recorded in host rock and some agates. Raman spectroscopy investigation was carried out using a dispersive Nicolet Almega XR Raman spectrometer (Thermo Fisher Scientific, Waltham, MA, USA) equipped with a 532 nm laser (Thermo Fisher Scientific, Waltham, MA, USA). The spectra were collected at 2 cm^{-1} spectral resolution. A confocal microscope with a 50 \times magnifying objective was used to direct the laser beam on the sample and to collect a Raman signal from a 2 μm diameter area. The Raman spectra of polished and thin sections of samples were acquired in the 85–4000 cm^{-1} region with an exposure time between 30 s and 100 s for each scan, depending on the signal intensity. The laser power was set from 2 to 10 mW to prevent sample degradation.

The Raman peak parameters (position, area, and width (i.e., full-width at half maximum (FWHM))), were measured using OMNIC for dispersive Raman software v.8.2. (Thermo Fisher Scientific, Waltham, MA, USA). For silica phases, the curve-fitting algorithm was used to fit the spectra with Lorentzian functions in the 400–550 cm^{-1} range using peaks of moganite at 502 cm^{-1} and quartz at 465 cm^{-1} . Moganite content was estimated using a calibration curve provided by Götze et al. [36]. The band protocol reported by Kouketsu et al. [37] was applied for peak decomposition of Raman spectra of carbonaceous matter. The Gaussian/Lorentzian function was applied for fitting.

The analysis of isotopic composition of carbonaceous matter from carbon-rich agate was carried out on powder samples at the Institute of Geology, Komi Science Center, Uralian Branch, Russian Academy of Sciences (IG Komi SC UB RAS, Syktyvkar, Russia). Organic carbon isotope measurement was carried out using a Flash EA1112 elemental analyzer coupled to a Thermo Delta V (Thermo Fisher Scientific, Bremen, Germany) isotope ratio mass spectrometer via a Conflo IV gas distribution system. The international standard USGS-40 (l-glutamic acid) and laboratory standard acetanilide (C₈H₉NO) were used. The $\delta^{13}\text{C}$ value is given in per mille relative to the VPDB (Vienna Pee Dee Belemnite) scale. The analytical precision was 0.15‰ (1 σ).

5. Results

5.1. Host Rock Characteristics

5.1.1. Organic Carbon-Rich Sedimentary Rocks

The studied rocks are mostly represented by massive siltstones of dark grey to black color. SEM-EDS petrographic study revealed microstructural heterogeneity of massive rock (Figure 4A,B). This is evident by irregular fine alternation of xenomorphic quartz grains, carbonaceous matter, and iron oxide inclusions. The quartz grain boundaries are unclear; grain size ranges from a few tens of micrometers to smaller. Micrometer-sized segregations of carbonaceous matter resemble a lithified liquid, which fills open space between quartz grains. Iron oxides occur predominantly as needle-like or laminar aggregates (Figure 4B). Accessory minerals are represented by chlorite, calcite, sericite, and sulfides.

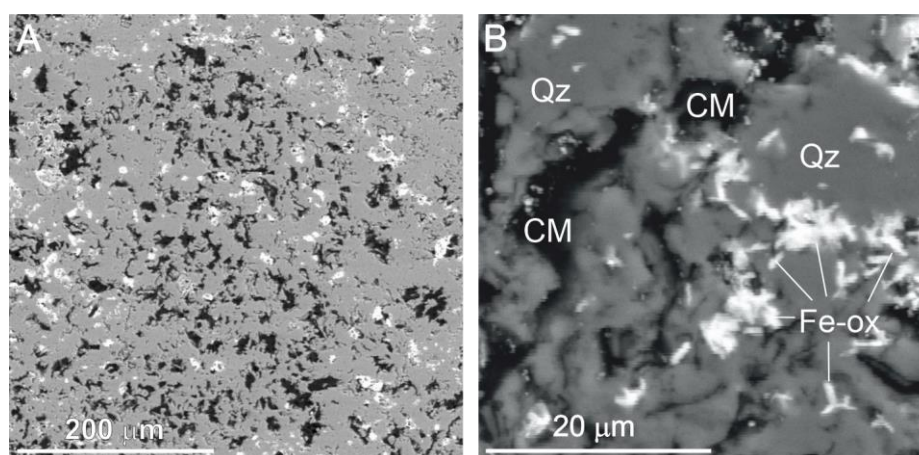


Figure 4. SEM-BSE images of increasing magnification (from (A) to (B)) illustrating microstructural heterogeneity of organic carbon-rich agate-bearing siltstone from the ZF of the Omega Basin. Black segregations—carbonaceous matter (CM), gray groundmass—quartz (Qz), light inclusions—iron oxides (Fe-ox).

The mineral composition of the host rock sample determined by XRD with Rietveld refinement is dominated by alpha quartz (91.1 wt.%), goethite (6.9 wt.%), and hematite (1.2 wt.%) (Figure S1). The wet chemical analysis shows high SiO₂ (83.24 wt.%) and total FeO (4.87 wt.%) contents, while the concentration of other major oxides is lower (Table S1). The high loss on ignition value (10.14 wt.%) is attributed to the presence of carbonaceous matter.

Differential thermal analysis was applied to determine carbon content in the host rock sample (Figure S2). The differential scanning calorimetry curve displays a strong exothermic maximum at 638 °C, which can be attributed to combustion of poorly ordered carbonaceous matter, e.g., coal or shungite [38,39]. The loss in mass resulting from combustion of carbonaceous matter is 9.67%.

5.1.2. Mineralized Agate-Bearing Veins

The studied rocks are fractured and contain veins mineralized by quartz, sulfides, iron oxides, and other low-temperature minerals. Veins vary in thickness from a few cm to 0.5 m, and their extension is up to 10–15 m. Locally, they form linear stockworks containing significant amounts of sulfides, hematite, and native sulfur (Figure 3D).

The most dominant sulfides are pyrite, sphalerite, and chalcopyrite, and typically occur as large crystals up to 1 cm in size and their aggregates (Figures 3D and 5B,G). Bornite, galena, and covellite were also recognized as microinclusions using SEM-EDS investigation (Figure 5A,C,F). Selenides were found in association with sulfides. Clausthalite (PbSe) forms grained aggregates and is replaced by rare minerals: tyrrelite (Cu,Co,Ni)₃Se₄ and cadmoselite CdSe (Figure 5D,E, Table S2). Relicts of clausthalite are preserved in newly

formed tyrrelite (Figure 5E). During oxidation, selenides are replaced by native selenium, and sulfides by hematite (Figure 5D); the native sulfur is segregated along cracks in sphalerite (Figure 5G). Secretion voids of ore aggregates are overgrown with acicular goethite crystals (Figure 5H). The occurrence of veinlets of the rare phosphate mineral corkite ($\text{PbFe}_3(\text{PO}_4)(\text{SO}_4)(\text{OH})_6$) associated with pyrite and hematite was revealed by EDS analysis, which showed the presence of 14.06 wt.% P_2O_5 , 7.10 wt.% SO_3 , 31.55 wt.% FeO , 1.52 wt.% As_2O_5 , and 29.99 wt.% PbO (Figure 5B). Accumulations of prismatic apatite grains were revealed in both quartz and hematite (Figure 5E,I).

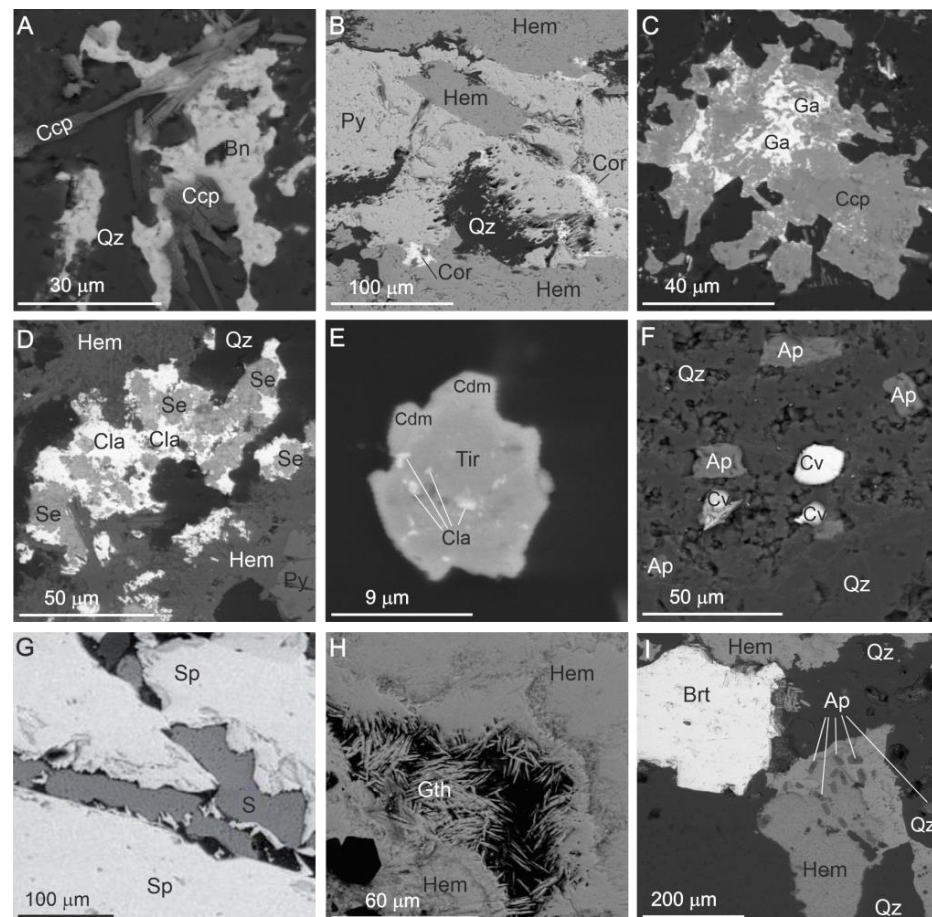


Figure 5. BSE images illustrating mineral composition of agate-bearing ore veins in the organic carbon-rich rocks. (A) Intergrowth of chalcopyrite (Ccp) and bornite (Bn); (B) corkite (Cor) veinlets associated with pyrite (Py) and hematite (Hem); (C) galena (Ga) accompanied by chalcopyrite aggregate; (D) clausenthalite (Cla) is replaced by native selenium (Se); (E) tyrrelite (Tir) with cadmoselite (Cdm) border and clausenthalite relicts; (F) inclusions of apatite (Ap) and covellite (Cv) accompanied by quartz (Qz); (G) veinlets of native sulfur (S) in sphalerite (Sp); (H) acicular goethite (Gth) crystals within the void of ore aggregate; (I) prismatic apatite grains in hematite associated with barite (Brt) and quartz.

5.2. Mineralogy of Agates

Textural and morphological characteristics of agates in the studied area are variable. Three main varieties of agates were identified, including concentrically zoned nodules, fine-banded agates, and carbon-rich moss agates.

5.2.1. Macro and Microscopic Characteristics

Concentrically zoned nodules are the most spectacular variety of agates recognized in organic carbon-rich host rocks (Figure 2). Nodules are spherical to subspherical in shape and range from 0.5 to 30 cm in diameter. They mainly exhibit monocentric zoning; polycen-

tric ones are also observed (Figure 2A). Nodules are characterized by rough bandings of mostly red, orange, and milky-white colors, and occasionally contain cavities encrusted by amethyst-like druses (Figure 2B). Frequently, they form groups controlled by thin quartz veinlets (Figure 2A,C). The outer boundary of the nodules at the point of contact with the host siltstone is uneven and wave-like.

Microscopic investigations revealed that red-orange areas of nodules formed by layers of length-fast (with *c*-axis oriented perpendicular to the fiber direction) and zebraic chalcedony (length-fast with a helical twisting of fibers along the fiber direction) (Figure 6A,C,E). These silica phases form rhythmic concentric bands, polygonal-shaped zones (Figure 6C), or rounded spherulites (Figure 6E). Fine-dispersed iron oxide particles disseminated within the chalcedony fibers are responsible for characteristic red-orange coloration of agates. Meanwhile, various color intensities of individual bands is observed. Additionally, randomly distributed globular or irregular iron oxide inclusions with a size of about 5–10 μm are present within the red-colored chalcedony zones (Figure 6D). Narrow bands with a thickness up to 20 μm containing a high concentration of iron oxide pigment sometimes mark the termination of individual zone crystallization (Figure 6D). The central colorless parts of some nodules are totally occupied by euhedral quartz crystals oriented with long axes perpendicular to the chalcedony layers (Figure 6A,B).

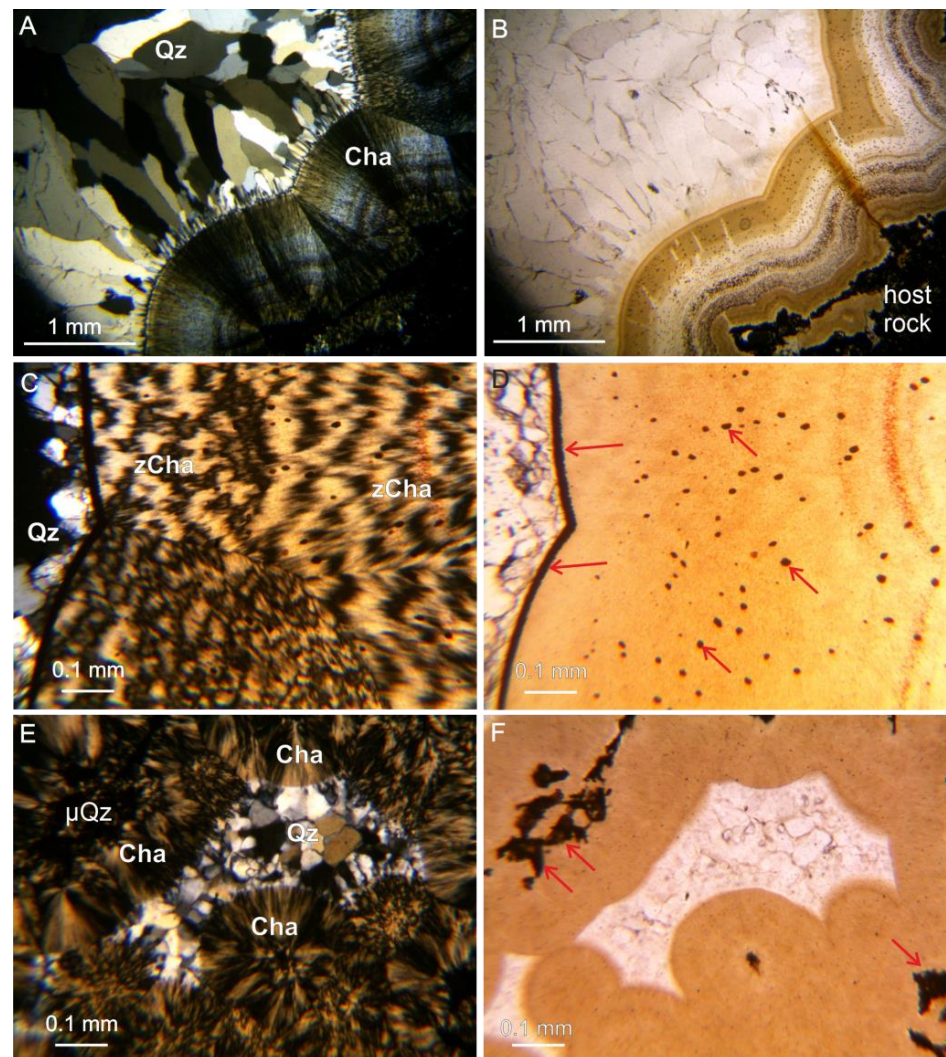


Figure 6. Microphotographs of concentric zoned nodules from the organic carbon-rich sedimentary rocks within the Onega Basin (LSH) ZF in transmitted light: (A,B) smooth transition from external banded chalcedonic area of the nodule with disseminated Fe-oxides compounds towards the

core comprising colorless prismatic quartz crystals; (C,D) polygonal-shaped aggregates of zebraic chalcedony at the point of contact with the inner nodule area comprising macrocrystalline quartz. Roundish dark inclusions occurred randomly arranged within the zebraic chalcedony band; (E,F) microgeode of macrocrystalline quartz surrounded by chalcedony spherulites and microcrystalline quartz. (A,C,E)—polarized light, crossed nicols; (B,D,F)—plane polarized light. The micrographs (B,D,F) show that the macroscopically visible orange color results from chromogenic Fe-oxides compounds disseminated within the individual bands of length-fast and zebraic chalcedony. Abbreviations: Cha, length-fast chalcedony; zCha, zebraic chalcedony; μ Qz, microcrystalline quartz; Qz, macrocrystalline quartz. The red arrows indicate the accumulations of Fe-oxide phases within the agate nodules.

According to the SEM-EDS observations, the most frequent iron oxide/hydroxide phases in the concentrically zoned nodule are expressed in the form of growths of needle-like crystals or irregular-shaped grains (Figure 7A–C). Infrequently, minute barite and microcline inclusions were recognized in the silica matrix (Figure 7A,B).

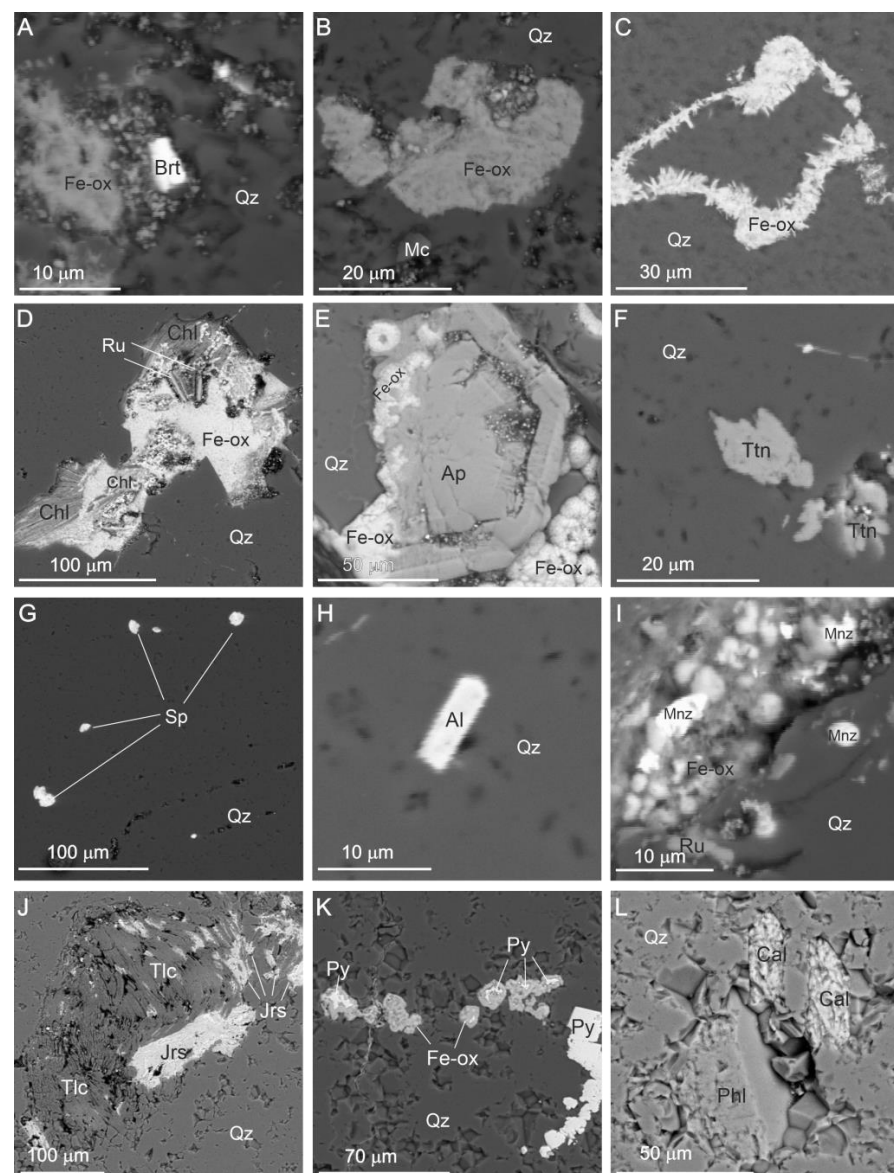


Figure 7. BSE images illustrating mineral composition of concentrically zoned nodule (A–C), fine-banded (D–I), and moss (J–L) agates from organic carbon-rich sedimentary rocks. (A) Inclusions

of barite (Brt) and iron oxide (Fe-ox) in quartz (Qz) matrix; **(B)** microcline (Mc) grain accompanied by quartz and iron oxide phase; **(C)** aggregates of growths of needle-like Fe-oxides in quartz matrix; **(D)** acicular rutile (Ru) inclusions associated with chlorite (Chl) and iron oxides; **(E)** skeletal apatite (Ap) crystal associated with spherical iron oxide aggregates; **(F)** titanite (Ttn) grains in quartz; **(G)** sphalerite (Sp) inclusions in quartz matrix; **(H)** allanite (Al) inclusion in quartz; **(I)** monazite (Mnz) inclusions associated with iron oxide veinlet; **(J)** lamellar aggregates of talc (Tlc) interbedded with jarosite (Jrs) segregations in quartz matrix; **(K)** accumulation of pyrite (Py) inclusions replaced by iron oxides; **(L)** inclusions of calcite (Cal) and phlogopite (Phl) in quartz.

Fine-banded agates occur within the mineralized quartz veins crosscutting organic-rich rocks (Figure 3A,B,D). Such agates exhibit both concentrically zoned (Figure 3A,D) and disordered (Figure 3B) textures represented as alternating red-, orange-, or yellow-colored bands and translucent zones. Fine-banded agates frequently contain cavities encrusted by quartz crystals (Figure 3D). The microstructure of the agates is predominantly represented by micro- and macrocrystalline quartz, and, to a lesser extent, by length-fast chalcedony (Figure 8A,C,E). These silica polymorphs form parallel-layered agate zones and fibrous radial aggregates. The inner zones of the BF agates are generally enriched in prismatic quartz crystals with a size of up to 1 mm along the c-axis (Figure 8E). A recurrent feature of prismatic crystals is the appearance of feathery microtextures exhibited under crossed polarizers (Figure 8C,E). These microtextures are characterized by subgrains, which appear as splintery or feathery patterns due to slight optical differences in maximum extinction positions [40]. The subgrains of feathery textures in the individual prismatic crystals are elongated parallel to each other in the crystal growth direction (Figure 8C). Furthermore, the quartz crystals with euhedral cores frequently exhibit feathery textures developed in the boundary of the crystals (Figure 8E). Wall-lining quartz crystals are locally characterized by the presence of numerous growth lines (Figure 8D–F) testifying to episodic stages of crystal growth (so-called Bombauer quartz) [41]. The growth lines are frequently colored by fine-dispersed iron oxide pigments (Figure 8D,F). Additionally, iron oxide/hydroxide phases are also aligned along the agate banding and emphasize micro-zoning (Figure 8B).

SEM-EDS investigation of fine-banded agates revealed various micromineral inclusions. Apart from Fe-oxide/hydroxide phases, they contain many plate-like chlorite crystals, which are responsible for the greenish color of individual agate layers (Figures 3A and 7D). The chemical composition of chlorite is characterized by high FeO (23.4–27.1 wt.%), MgO (7.6–12.8 wt.%), and ZnO (up to 5.9 wt.%) contents. Needle-like V-enriched (up to 4.7 wt.% V₂O₅) rutile crystals were occasionally observed in association with chlorite and Fe-oxide phases (Figure 7D). Hydroxylapatite is represented by skeletal crystals with distinct crystalline contours, up to 100 µm in cross-section (Figure 7E). Sporadic xenomorphic grains of titanite up to 20 µm in size and Cd-enriched (up to 6.9 wt.%) sphalerite inclusions with sizes of 5–20 µm were recognized in the silica matrix (Figure 7F,G). REE-bearing minerals were revealed as both single grains in quartz and clusters associated with Fe-oxide phases. The chemical composition of prismatic grains (20.71 wt.% Al₂O₃, 41.90 wt.% SiO₂, 15.58 wt.% CaO, 9.11 wt.% FeO, 4.68 wt.% La₂O₃, 8.03 wt.% Ce₂O₃) occurring within the silica mass is close to allanite (Figure 7H). The composition of xenomorphic grains (38.21 wt.% P₂O₅, 17.83 wt.% La₂O₃, 32.82 wt.% Ce₂O₃, 10.52 wt.% Nd₂O₃) suggest the presence of monazite (Figure 7I).

Moss agates occur as infills of fissures and cracks within the organic carbon-rich siltstones. They form veins and veinlets and often coexist with smoky quartz druses (Figure 3C). Moss agates are represented by coarse-grained quartz aggregates, strongly impregnated with carbonaceous matter and Fe-oxide impurities, which determine their smoky-brownish color (Figure 3C). The microscopical study in cross-polarized light revealed that moss agates are characterized by patchy zoning represented mostly by rounded patches (1–4 mm in diameter) of microcrystalline quartz grains within the macrocrystalline quartz matrix (Figure 9A). Polygonal aggregates of macrocrystalline quartz embedded

in an area of microcrystalline quartz were also observed (Figure 9B). The carbonaceous matter in moss agates forms irregular segregations within the microcrystalline quartz matrix and tends to accumulate with other accessory minerals such as mica and iron oxides (Figure 9C,D).

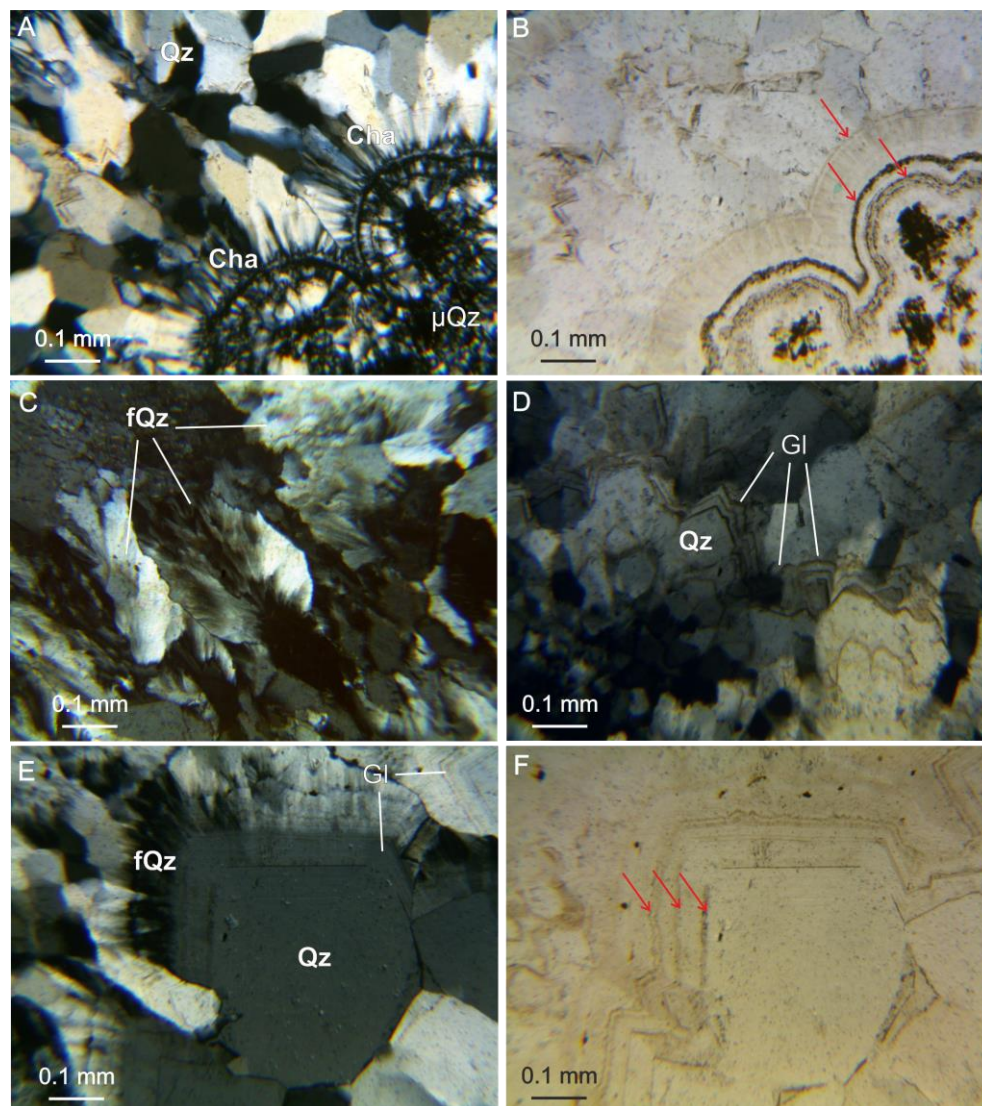


Figure 8. Microphotographs of fine-banded agates from the ZF organic carbon-rich rocks within the Onega Basin in transmitted light: (A,B) different generations of silica forming the banding; (C) internal part of the agate occupied by euhedral prismatic quartz with feathery microtextures developed within the crystals; (D) growth lines (so-called Bambauer quartz) developed within the quartz crystals and impregnated by Fe-oxides; (E,F) euhedral quartz crystal with growth lines and feathery texture developed in the boundary of the crystal. (A,C–E)—polarized light, crossed nicols; (B,F)—plane polarized light. Abbreviations: Cha, length-fast chalcedony; μ Qz, microcrystalline quartz; Qz, macrocrystalline quartz; fQz, feathery quartz; Gl, growth lines. The red arrows indicate the accumulations of Fe-oxide phases.

SEM-EDS analysis indicates that moss agates comprise lamellar aggregates of talc, and inclusions of calcite, dolomite, and phlogopite (Figure 7J,L). Pyrite inclusions occur as clusters of prismatic or irregular grains in quartz matrix (Figure 7K). They frequently exhibit microheterogeneity resulting from iron oxide substitution of the sulfide phase. The composition of irregular segregations (SO_3 35.4 wt.%, K_2O 9.7 wt.%, FeO 44.31 wt.%)

associated with talc most likely corresponds to jarosite ($\text{KFe}_3(\text{SO}_4)_2(\text{OH})_6$) (Figure 7J). In places, it is replaced by iron oxides.

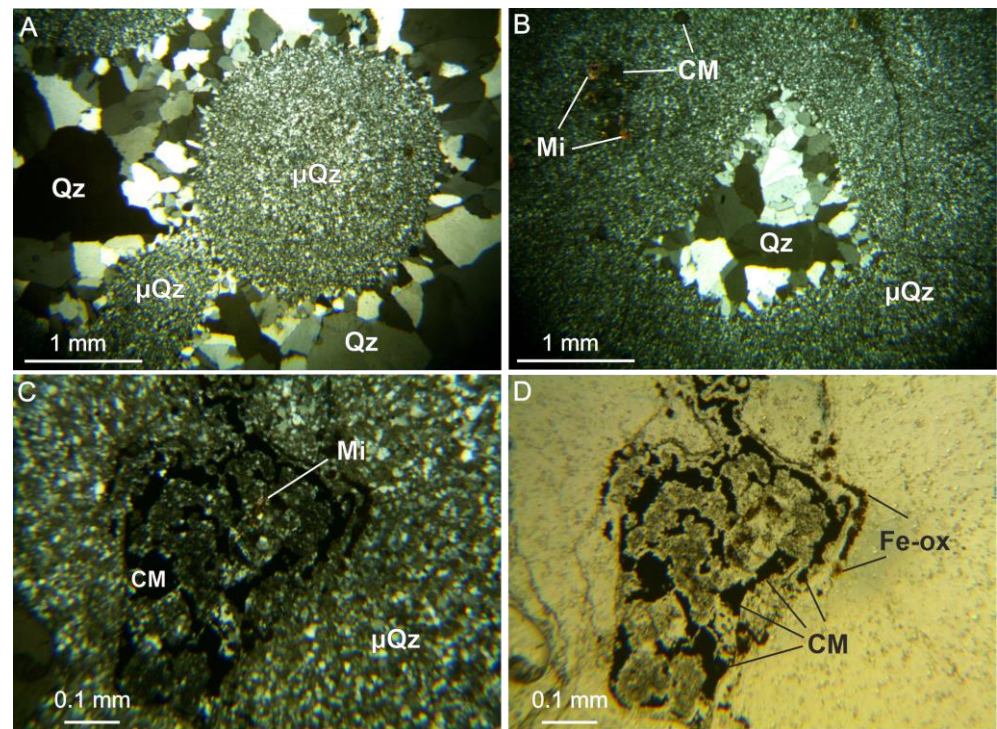


Figure 9. Microphotographs of moss agates from the ZF organic carbon-rich rocks within the Omega Basin in transmitted light: (A) rounded patches of microcrystalline quartz (μQz) grains within the macrocrystalline quartz (Qz) matrix; (B) polygonal aggregate of macrocrystalline quartz occupied by microcrystalline quartz associated with inclusions of mica and carbonaceous matter (CM); (C,D) accumulation of carbonaceous matter, Fe-oxides (Fe-ox), and mica (Mi) inclusions within the macrocrystalline quartz area. (A–C)—polarized light, crossed nicols; (D)—plane polarized light.

5.2.2. X-ray Diffraction

The phase composition of three bulk samples (concentrically zoned nodule, fine-banded, and moss agates) was examined by the powder XRD method. Reflections corresponding to α -quartz have been identified in all the XRD patterns. Analysis of the diffractogram of the concentrically zoned nodule suggests the occurrence of admixtures of silica polymorph moganite in the sample. It is evidenced by the small shoulders at the base of the quartz reflections at about 2θ 20° and 26° (Figure S1). Additionally, diffractograms of the concentrically zoned nodule and fine-banded agate contained weak peaks of goethite and/or hematite (Figure S1).

The differences in the XRD patterns of examined agates are also a minor broadening and variations in the intensities of some quartz reflections. The differences in the degree of resolution of the (212) reflection at about 2θ 67.8° were used for the calculation of a quartz crystallinity index (CI) of examined samples according to the equation $\text{CI} = 10 \text{ Fa}/\text{b}$ (Figure 10) [42]. A clear euhedral quartz crystal from hydrothermal veins of the Subpolar Urals (Russia) [43] served as a standard sample with $\text{CI} = 10$. The scaling factor F was 1.2. XRD patterns of fine-banded and moss agates display a well-resolved quintuple peak at about 2θ 68° (Figure 10). CI values for these samples were estimated at 8.4 and 9.0, respectively. In contrast, the concentrically zoned nodule is characterized by a broader and more diffuse XRD pattern and a lower CI value (3.0) (Figure 10, Table 1).

The mean crystallite size (C_s) of the samples was estimated using the Scherrer equation: $C_s = K\lambda/(\cos\theta)$. The shape factor K was taken as 0.9, λ was the wavelength of Cu-K α 1 radiation (1.540562 Å), and β was the full width at the half maximum of the reflection

(101) at 2θ 26.6°. Cs (101) was taken to be representative of the average crystallite diameter. The fine-banded and moss agates exhibited higher mean crystallite sizes (741 and 799 Å, respectively) as compared to the concentrically zoned nodule with a Cs of 425 Å (Table 1).

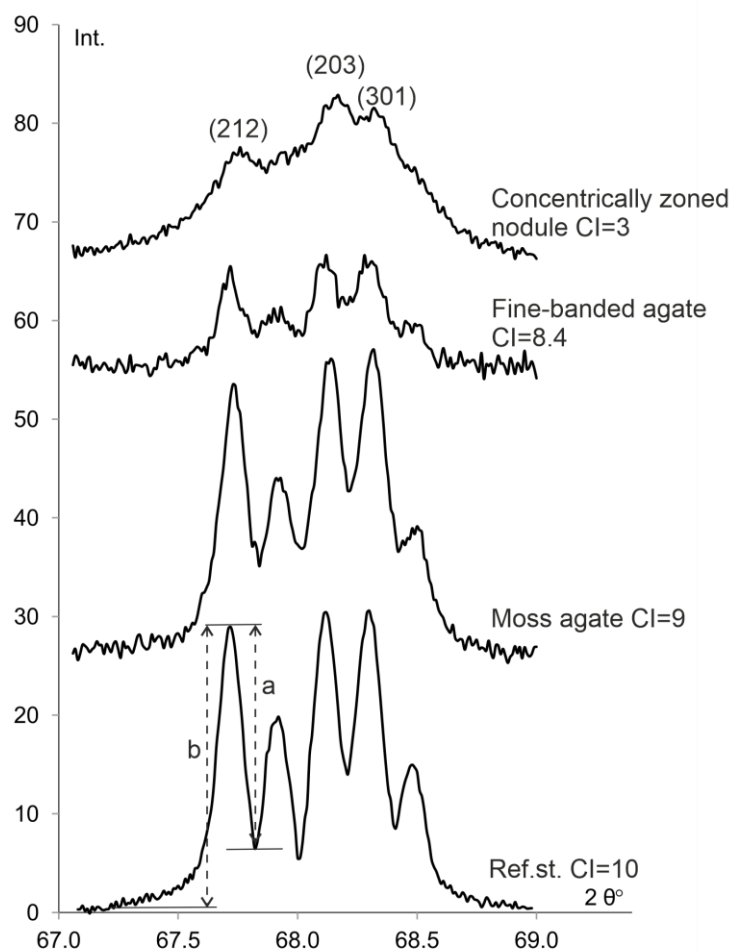


Figure 10. Selected sections of XRD patterns with the 2θ 68° quintuple peak of the concentrically zoned, fine-banded, moss agates and standard sample (Ref. st., quartz crystal, Subpolar Urals). a and b—parameters for crystallinity index (CI) calculation.

Table 1. Crystallite size (Cs) and crystallinity index (CI) of α -quartz from agates.

Sample	Cs, Å	CI
Concentrically zoned nodule	425	3.0
Fine-banded agate	741	8.4
Moss agate	799	9.0
Quartz crystal, ref. std.	935	10

5.3. Raman Spectroscopy Results

5.3.1. Content and Occurrence of Moganite in Agates

Raman micro-spectroscopy analyses confirmed the presence of moganite phases in the concentrically zoned nodule, which have been identified using its main Raman band located at 502–503 cm^{-1} [36]. This band, together with characteristic α -quartz bands at 465, 353, 208, and 127 cm^{-1} [36], were recognized in all Raman spectra collected from length-fast chalcedony layers (Figure 11A,C). It is noteworthy that zebraic chalcedony and macrocrystalline quartz areas of the sample were moganite-free.

The moganite band at 502 cm^{-1} combined with α -quartz bands was also recognized in the Raman spectra collected from feathery texture areas bordering euhedral quartz crystals

within the fine-banded agate (Figure 11B,C). The Raman spectra of length-fast chalcedony layers of fine-banded agate show low-intensity moganite bands in rare cases. According to our data, moganite is absent in the areas composed of micro- and macrocrystalline quartz, including euhedral quartz crystals (Figure 11B,C). No moganite has been found within the moss agates.

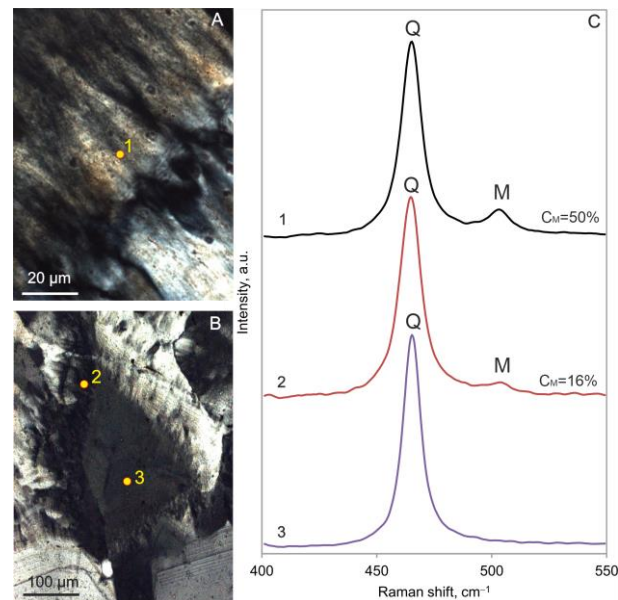


Figure 11. Microphotographs in cross-polarized light and Raman spectra of local analyses of fibrous chalcedony areas from concentrically zoned agate (A,C) and euhedral quartz crystal with feathery appearance from fine-banded agate (B,C). Raman spectra (1–3) in (C) correspond to analytical spots, which are marked by yellow circles on the photos. Spectra (1, 2) display the main characteristic bands of α -quartz (Q) at 465 cm^{-1} and moganite (M) at 502 cm^{-1} , while spectrum (3) shows only the α -quartz band. C_M is calculated moganite content.

To quantify local moganite content in moganite-rich areas of concentrically zoned nodules and fine-banded agate, we applied an algorithm based on the evaluation of the intensity ratio of moganite and α -quartz Raman bands $I_{(502)}/I_{(465)}$ proposed by Götze et al. [36]. The estimated intensity ratios $I_{(502)}/I_{(465)}$ for length-fast chalcedony layers of concentrically zoned nodules range between 4.6% and 19.7% (Table S3). According to the calibration curve [36], these values correspond to local moganite content of 22%–50%. For feathery texture areas within the fine-banded agate, the intensity ratio $I_{(502)}/I_{(465)}$ did not exceed 3.5%, corresponding to a moganite content of up to 16% (Table S3).

5.3.2. Characteristics of Carbonaceous Matter

Carbonaceous matter is present in both moss agate and agate-bearing siltstone. The Raman spectra of carbonaceous matter in the moss agate and agate-bearing rock samples are similar and correspond to poorly ordered carbonaceous matter [44–48]. This is evident from two well-resolved intensive bands: D1 at about 1350 cm^{-1} and G band at about 1600 cm^{-1} in the first-order region of the Raman spectra (Figure 12A,C). In the second-order region of the Raman spectra, carbonaceous matter from both moss agate and host rock samples are mainly characterized by weak bands located at 2700 and 2950 cm^{-1} (Figure 12A,C).

The decomposition of Raman spectra of carbonaceous matter in the first-order region shows the occurrence of an additional low-intensity disorder-related band D4 ($\sim 1260\text{ cm}^{-1}$) (Table S4). The D3 band ($\sim 1500\text{ cm}^{-1}$) was established only in a few Raman spectra of carbonaceous matter from moss agate, while the D2 band ($\sim 1620\text{ cm}^{-1}$), which appeared in

relatively ordered carbonaceous material [44–48], is totally absent in the Raman spectra of carbonaceous matter from both moss agate and host rock samples (Table S4).

The most sensible Raman spectra parameters—the full width at half maximum of D1 band (FWHM-D1) and intensity-based $R1 = ID1/IG$ [37,45,49] ratio—were used to characterize the degree of structural ordering of carbonaceous matter recorded in examined samples (Table S4). Carbonaceous matter from host rock samples is characterized by $R1 = 0.86–1.22$ (av. 1.07) and $FWHM-D1 = 79–108\text{ cm}^{-1}$ (av. 94 cm^{-1}). Carbonaceous matter from moss agate has similar average values of $R1$ (1.10) and $FWHM-D1$ (93 cm^{-1}). However, the scattering of their spectral parameters ($R1 = 0.76–1.38$, $FWHM-D1 = 67–108\text{ cm}^{-1}$) is slightly higher compared to the host rock sample. Overall, high average values of $R1$ close to 1 accompanied with the high average values $FWHM-D1 = 93–94\text{ cm}^{-1}$ and low intensive (or absent) disorder-related bands D3 and D4 are indicative of medium-grade carbonaceous matter in the examined samples, according to the classification proposed by Kouketsu et al. [37].

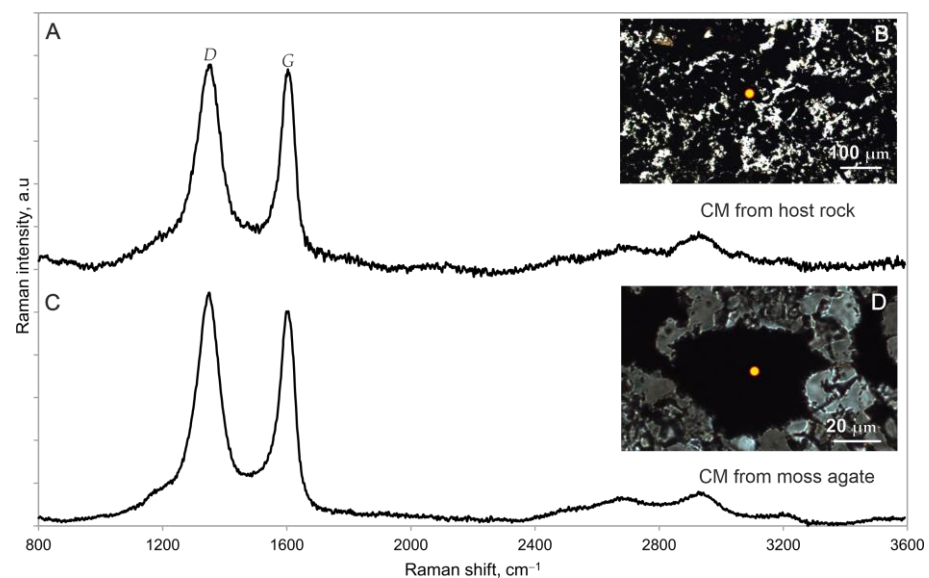


Figure 12. Representative Raman spectra and micrographs of carbonaceous matter (CM) in organic carbon-rich host rock (A,B) and moss agate (C,D) in the range of $800–3600\text{ cm}^{-1}$. Analytical points are marked by yellow circles on the photos. (B)—plane polarized light, (D)—cross-polarized light.

The empirical Raman geothermometer of Kouketsu et al. [37] was applied to assess the metamorphic temperatures of carbonaceous matter. This thermometer is based on the principle that the structural ordering of carbonaceous matter is an irreversible process, so the degree of graphitization is an indicator of the maximum temperature of metamorphic transformation, i.e., the structure and the microstructure of carbonaceous matter are unaffected by retro-grade metamorphic events [49,50]. The resulting temperature range of thermal transformation for carbonaceous matter in moss agate and host rock was ca. $240–330\text{ °C}$ (Table S4). These temperatures correspond to the prehnite-pumpellyite facies and are consistent with results of previous studies [14].

5.3.3. Characteristics of Iron Mineral Inclusions

The major Fe-oxide/hydroxide minerals occurring in agates were identified as goethite and hematite. Rounded yellowish inclusions (revealed in reflected light) randomly arranged within the orange chalcedony bands were evidenced as goethite by their characteristic Raman bands at $385, 417, 551, \text{ and } 684\text{ cm}^{-1}$ (Figure 13) [51,52]. Raman spectra of fine-dispersed reddish inclusions within the same bands exhibit main hematite bands located at $411, 610, 660, \text{ and } 1321\text{ cm}^{-1}$ [51,53], and additionally show the chalcedony matrix (Figure 13). It is evident from the alpha quartz (465 cm^{-1}) and moganite (502 cm^{-1})

bands. The Raman spectra recorded for iron oxide inclusions associated with carbonaceous matter within the moss agate (Figure 8D) revealed only the presence of goethite bands.

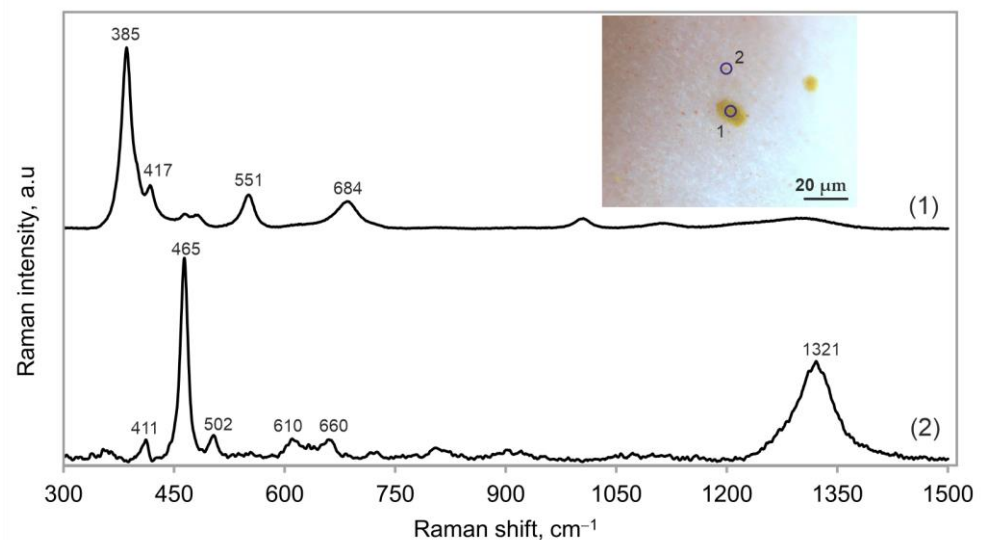


Figure 13. Micrograph in reflected light and Raman spectra of goethite (1) and hematite (2) located within the orange chalcedony band of a concentrically zoned nodule in the range of 300–1500 cm^{-1} . Analytical points 1, 2 are marked by circles on the photo. Bands at 465 and 502 cm^{-1} on spectrum (2) correspond to alpha quartz and moganite, respectively.

5.4. Carbon Isotope Composition

Analysis of the isotopic composition of the carbon was carried out to obtain additional information about the origin of the carbonaceous matter in moss agate. A fragment of moss agate enriched with carbonaceous matter was used. The measured $\delta^{13}\text{C}_{\text{org}}$ value of -25.64‰ suggests a biogenic source of carbon.

6. Discussion

Existing studies of agates formed in sedimentary settings are very limited. The majority of such agates are found in limestones and are essentially related to Phanerozoic rocks [54–58]. The agate occurrence considered in this paper is unique in that it is confined to Paleoproterozoic sedimentary rocks. The agate host rocks are represented by carbon-bearing siltstones (with a carbon content of about 10%) aged 2050 Ma [27]. A distinctive lithological characteristic of rocks is the local occurrence of diagenetic nodules of calcite and dolomite composition [1]. The studied locality in the vicinity of Kondaberezhskaya village is currently the only known agate occurrence associated with sedimentary rocks of the Onega Basin. It can be assumed that the examined Paleoproterozoic rocks are the oldest agate-bearing sediments described in the scientific literature.

6.1. Morphology, Microtexture, and Silica Composition of Agates

Agates have been recognized as rounded nodules in organic carbon-rich siltstones, as well as infills of tectonic fissures and cavities in these rocks. Three morphological varieties of agates were distinguished, including concentrically zoned nodules, fine-banded agates, and carbon-rich moss agates. The agates exhibit various silica microtextures due to individual zones composed of micro- and macrocrystalline quartz, and length-fast and zebraic chalcedony. The appearance of Bambauer quartz with typical growth lines within agates (Figure 8E,F) indicates a lower temperature of mineralizing fluids characterized by strong fluctuations in pH conditions and/or silica content [41,58–60]. The feathery microtextures revealed within agates (Figure 8C,E) are typical of quartz from epithermal system and have been described for agates in a number of deposits (e.g., [59–61]). The

presence of these textures is evidence for recrystallization from water-rich microcrystalline silica polymorphs (moganite and/or chalcedony) [62–64].

The intergrowth of moganite with chalcedony is frequent in agates [36,65,66]. Spatial distribution of moganite within banded agates is not homogenous. Both moganite-rich and moganite-free chalcedony areas of agates have been observed [61,67–69]. Moxon and co-authors investigated agates from varying hosts and revealed a relationship between the age of agate host rocks and corresponding moganite content in the agates [65,70,71]. Moganite is consistently recognized in agates found in hosts aged up to 400 Ma. The amount of moganite sharply decreases with the increasing age of host rocks from 13 to 60 Ma, and then remains approximately constant up to 400 Ma. In the older agates from host rocks aged between 400 and 1100 Ma, moganite occurs in trace amounts or is not detected. No moganite has been detected in ancient agates aged more than 1100 Ma [72]. The agates from Proterozoic volcanic rocks within the Onega and Pasha-Ladoga Basins are also moganite-free [13,73]. It is assumed that decreasing moganite content in agates with respect to host age is due to the release of structural silanol water over the geological time scale, and transformation of metastable moganite phases into quartz [66]. Therefore, the high moganite content in individual areas within examined concentrically zoned nodules (up to 50%) and trace amounts of moganite in fine-banded agate is unexpected for agates hosted in Paleoproterozoic (ca. 2050 Ma) rocks.

The same applies to the obtained data on the main crystallite size and the crystallinity index of the examined agates. A positive correlation between the main crystallite size of the agates and age of the host rocks was provided by Moxon [74]. The measured values of Cs (425 Å) and CI (3) for concentrically zoned nodules are significantly different from those obtained for fine-banded and moss agates (Cs: 741, 799 Å; CI: 8.4, 9, respectively) hosted in the same rocks. It should be noted that agates from similarly aged Paleoproterozoic volcanics of the Onega Basin are characterized by Cs = 710–1050 Å and CI > 8 [13]. It is suggested that an increasing of crystallite size and crystallinity index in agates is the result of the transformation of fibrous silica phases (chalcedony and moganite) to granular alpha quartz during late metamorphic alteration [70].

Combined, the high moganite abundance and low Cs and CI values in concentrically zoned nodules are characteristics of ‘immature’ agates that have not undergone significant metamorphic effects. Overall, this evidence indicates that formation of nodules within the organic carbon-rich rocks took place long after both the deposition of the sedimentary sequence and the formation of the fine-banded and moss agates. Meanwhile, carbon-rich moss agates, in which metastable silica phases (moganite and chalcedony) were not found, are most likely older compared to fine-banded agates, where relics of chalcedony were preserved (Figure 8A) and a trace amount of moganite was revealed within the feathery texture areas bordering euhedral quartz crystals (Figure 11B,C).

Fine-banded and moss agates associated with veins are similar in structural parameters (Cs and CI) to agates found in volcanic rocks of the Onega Basin [13,14]. A distinctive characteristic of fine-banded agate compared to agates from volcanics is the presence of insignificant moganite impurities and an abundance of iron oxides and hydroxides, indicating the significant role of iron in the agate-forming environment.

6.2. Mineral Assemblage of Agate-Bearing Veins and Agates

Agate vein mineralization in the study area is widely accompanied by other products of hydrothermal activities such as sulfides, selenides, carbonates, sulfates, iron oxides, native sulfur, etc. (Table 2). Sulfide minerals are dominated by pyrite, chalcopyrite, and sphalerite with lesser amounts of galena, bornite, and covellite. Of note is the finding of rare selenides, such as clausthalite, tyrrellite, and cadmoselite. The appearance of native selenium and sulfur is obviously related to supergene alteration of clausthalite and sphalerite, respectively, while corkite is probably originated by alteration of polysulfide aggregates.

The studied agate occurrence is located at the Zaonega Peninsula (Figure 1B), which is particularly famous for its numerous ore objects with noble metal mineralization. The

most significant are Cu-(noble metals)-V-U Srednyaya and Verchnyaya Padma, Tsarevskoe, and Vesennee deposits (Padma group) [11,12]. Several U-V-ore objects containing vein-disseminated noble-metal-sulfide-selenide mineralization also occur. They are represented by the Kosmozero deposit, South Kosmozero, and Velikaya Guba occurrences, united in the Kosmozero group [12]. Their placement is controlled by the Svyatukha-Kosmozero fold-fault deformation zone and intense alkaline-micaceous alteration of rocks. Most U-V ore deposits are associated with carbonate-micaceous-albite metasomatites after siltstones and dolomites [12]. Our studies show that the deposition of vein agates is associated with ore systems formation (Kosmozero and Padma groups) and took place during the orogenic stage within the Paleoproterozoic complexes of the Karelian Craton [12].

Table 2. Summary of mineral assemblages of agates and agate-bearing ore veins.

Type of Mineralization	Silica Phases	Mineral Assemblage
Fine-banded agate	Micro- and macrocrystalline quartz, chalcedony, moganite (trace amount)	hematite, goethite, chlorite (Zn), apatite, titanite, barite, pyrite, sphalerite (Cd), rutile (V), allanite, monazite
Moss agate	Micro- and macrocrystalline quartz, smoky quartz	carbonaceous matter, goethite, calcite, dolomite, talc, pyrite, jarosite, phlogopite
Concentrically zoned nodule	length-fast and zebraic chalcedony, micro- and macrocrystalline quartz, amethyst, moganite	hematite, goethite, and barite
Stockwork mineralization	macrocrystalline quartz	hematite, goethite, pyrite, bornite, chalcocopyrite, galena, sphalerite, covellite, apatite (F), barite, ilmenite, albite, clausthalite, tyrellite, corkite, native selenium, cadmoselite, native sulfur, jarosite, calcite

An abundance of apatite grains was observed in the agate-bearing ore veins. Additionally, skeletal apatite crystals were directly recognized in fine-banded agate. Previously, phosphorus-rich intervals with abundantly occurring apatite were found within the organic carbon-rich sediments in the upper part of the ZF [75]. It is concluded that phosphatic sediments in the Paleoproterozoic Zaonega Formation record phosphogenesis in a vent/seep influenced setting that experienced fluctuating redox conditions at the sediment-water interface [75].

A common feature of all varieties of studied agates is the presence of iron oxide/hydroxide compounds, indicating the activity of iron in the agate-forming fluids (Table 2). Disseminated hematite inclusions in the silica matrix are predominantly responsible for the reddish color of nodules and fine-banded agates. Various morphologies of the particles and their concentration cause the differing color tints of individual agate bands. Goethite is responsible for the yellow-brownish agate color.

The vein varieties of agates (fine-banded and moss agates) in contrast to concentrically zoned nodules contain diversified accessory minerals, such as pyrite, sphalerite, barite, calcite, dolomite, apatite, chlorite, titanite, talc, phlogopite, allanite, monazite, rutile, and jarosite (Table 2, Figure 6), which were probably formed during the post-magmatic and metamorphic processes.

A distinctive feature of moss agate is the presence of carbonaceous matter. Solid inclusions of carbonaceous matter in agates are a rarity. They have been identified in agates from Permian acid volcanic rocks in the vicinity of Nowy Kościół (Lower Silesia, Poland) [76], Triassic basalts of the Meknés-Tafilalet, Asni, and Agouim Regions (Morocco) [60,77], and onyx agates from Mali [78]. The origin of carbonaceous matter in agates is uncertain. For example, it is assumed that the inclusions of carbonaceous matter in Mali agates might originate from both the hydrothermal formation of graphite from methane under elevated temperature, and graphitization of organic precursors by secondary hydrothermal and metamorphic overprint [78]. The stable carbon isotope analysis of the solid hydrocarbon (bitumen) substance in agates from Nowy Kościół revealed its algal or algal-humic origin [76].

Carbonaceous matter was also recognized in the black agates from volcanics confined to the LSH within the Onega Basin [14]. It is suggested that the source of carbonaceous matter in these agates could be hydrothermal fluids enriched in mechanically derived carbonaceous matter incorporated from underlying organic carbon-rich sedimentary rocks.

Raman spectroscopy data show that carbonaceous matter recorded in examined moss agate and organic carbon-rich host rock is similar and corresponds to poorly ordered carbonaceous matter. The significant scattering of both spectral parameters R1 and FWHM-D1 indicates the high degree of heterogeneity of carbonaceous matter (Figure 14). It is noteworthy that carbonaceous matter from previously studied black agates hosted in LSH volcanic rocks has a similar FWHM-D1 parameter and slightly lower values of the R1 parameter (with high scattering of both parameters) compared to carbonaceous matter recorded in moss agate and host rock (Figure 14) [14]. Moreover, carbonaceous matter from the organic carbon-rich ZF sedimentary rocks unaffected by hydrothermal alteration of some localities [79] is characterized by a significantly higher degree of structural order compared to carbonaceous matter from moss agate and host rock. This is evident from high values of R1 (av. 1.3–1.64) combined with low FWHM-D1 (av. 44–57 cm^{-1}) (Figure 14). Chazhengina and Kovalevsky [79] have shown that weathering processes result in changes of carbonaceous matter ordering of rocks. However, mechanisms of degradation of carbonaceous matter depend on the type of weathering (physical, chemical, biogenic) that is reflected in the changes of Raman spectra. A comparative analysis of the Raman parameters of carbonaceous matter from rocks subjected to hydrothermal alteration (moss agates, organic carbon-rich agate-bearing siltstone, and black agates from LSH volcanics) and unaltered organic carbon-rich rocks suggests that the decrease in structural order of carbonaceous matter could be caused by local hydrothermal alteration of the rocks, which led to disorder of carbonaceous matter (Figure 14).

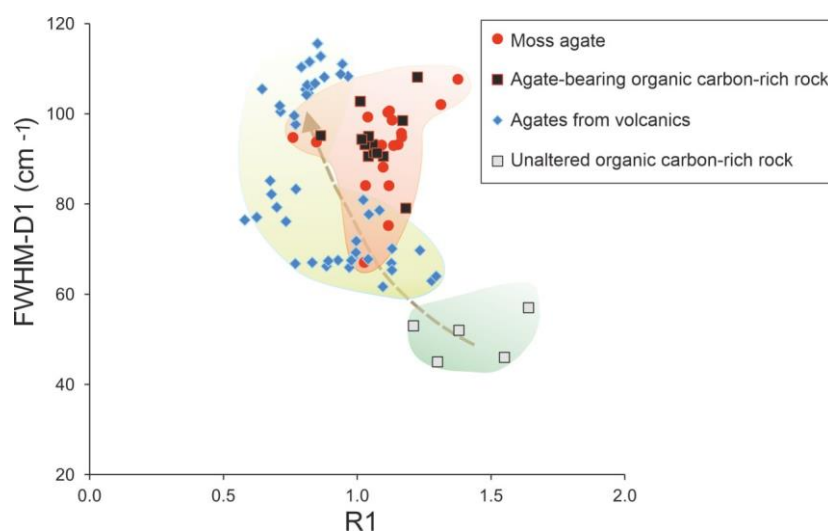


Figure 14. R1 versus FWHM-D1 plot for carbonaceous matter from moss agates and agate-bearing organic carbon-rich rocks obtained in the present study compared to data for black agates from LSH volcanic rocks [14] and unaltered organic carbon-rich LSH sedimentary rocks [79]. The arrow shows the proposed trend of Raman parameter changes caused by hydrothermal alteration.

The carbon isotope composition of crustal rocks is generally considered an indicator of the source of carbonaceous matter due to significant differences between biogenic and mantle carbon. Typical mantle $\delta^{13}\text{C}_{\text{org}}$ values are ca. -5% [80] while lower values are interpreted as biogenic carbon or as a result of mixing of biogenic and mantle carbon. The $\delta^{13}\text{C}_{\text{org}}$ can also be modified because of metamorphic alteration [4,81]. The measured $\delta^{13}\text{C}_{\text{org}}$ value of -25.64% of the carbonaceous matter in the studied moss agate is compatible with the values (-25.59% ... -28.07%) of the black agates from the LSH volcanic rocks, and suggests an organic precursor for the carbonaceous material (Table 3). These values

are within the range of organic carbon-rich rocks (siltstones, sandstones, interbed and vein pyrobitumen) of the ZF (−17 to −46‰) [24,25], suggesting a similar source.

Table 3. $\delta^{13}\text{C}_{\text{org}}$ values of carbonaceous matter occurring within the agates and organic carbon-rich rocks of the LSH within the Onega Basin.

Characteristics	$\delta^{13}\text{C}$, ‰ V-PDB	References
Moss agate from organic carbon-rich sedimentary rocks	−25.64	Our data
Black agates from volcanic rocks	−25.59...−28.07	Authors' personal data
Vein pyrobitumen	−24...−38	[24]
Interbed pyrobitumen	−36...−46	[6]
organic carbon-rich siltstones, sandstones	−17...−44	[25]

6.3. Origin of Concentrically Zoned Nodules

The origin of the agates in sedimentary rocks is often related to the pseudomorphic substitutions of carbonate or sulphate concretions distributed in the limestone or calcareous sandstone sequences [54,55,57,82,83]. Macroscopically, these pseudomorphized concretions have external rounded protuberances similar to a head of cauliflower [56,58,82]. Mineral species such as carbonates (calcite, dolomite) or sulphates (anhydrite, celestine), being more soluble than host rocks, have been in large part removed, thus affording cavities in which the agates could be formed. Where they are still preserved, the concretions have exactly the same relationship to the host rock as the agates and possess analogous shapes [54]. Huge areas containing agates, chalcedony, and quartz geodes, which are replacement concretions, are known in many sedimentary sequences of varying ages worldwide. Examples are the Fairburn agates from the Minnelusa Formation (SD, USA), Dryhead agates from the Phosphoria Formation (MT, USA), quartz geodes known as “Bristol diamonds” of the Bristol district (UK), geodes from Warsaw, Keokuk, Fort Payne, Ramp Creek Formations (USA), geodes from the Basque-Cantabrian Basin (Spain), and silica nodules from limestones of Moscow region (Russia) [55–57,82–88].

The abundance of diagenetic concretions of calcite-dolomite composition locally observed within the studied sedimentary rocks [1] and morphology of the examined agate nodules suggest that they could be formed due to the dissolution of carbonate concretions and their silicification as a result of late hydrothermal processes. Silicification started on the walls of nodules and continued inward, toward the nodule center. After the outer part of the carbonate nodules was replaced by chalcedony, the silica-enriched fluids became less concentrated, resulting in the dissolution of the remaining carbonate. This produced the central cavity in which macrocrystalline quartz precipitated. Hydrothermal fluid is the most likely source of silica. Similar assumptions about the participation of hydrothermal fluid in formation of agates from the Dryhead area (Montana, USA) occurring in Permian sedimentary rocks (clay shale and siltstone) were reported by J. Götze et al. [83]. The analysis of published data on the homogenization temperatures of fluid inclusions in agates containing moganite, microcrystalline and crystalline alpha quartz shows that the formation temperatures of such agates do not exceed 200 °C. For example, the fluid inclusions study of moganite-rich agates of volcanic complexes (Kamchatka, Russia) shows that the crystalline quartz in the center of the nodule in agates was formed in the temperature range 110–50 °C and below [61,89]. The fluid inclusion study of agates from placer deposits of China shows that the formation temperatures of the silica sequence (moganite-rich pseudo-granular silica → fibrous chalcedony → crystalline quartz) are 120–170 °C [90]. The hydrothermal fluids that formed the examined agate nodules with similar silica composition were apparently also low-temperature.

6.4. Origin of Agates in Organic Carbon-Rich Rock in the Omega Basin

Summarizing the results of mineralogical investigation of agates obtained in the present study and data of a previous study of agates from volcanic rocks of the LSH, as well as analysis of regional geological material, the agate mineralization in LSH within the Omega Basin can be generalized into five stages, as illustrated in Figure 15.

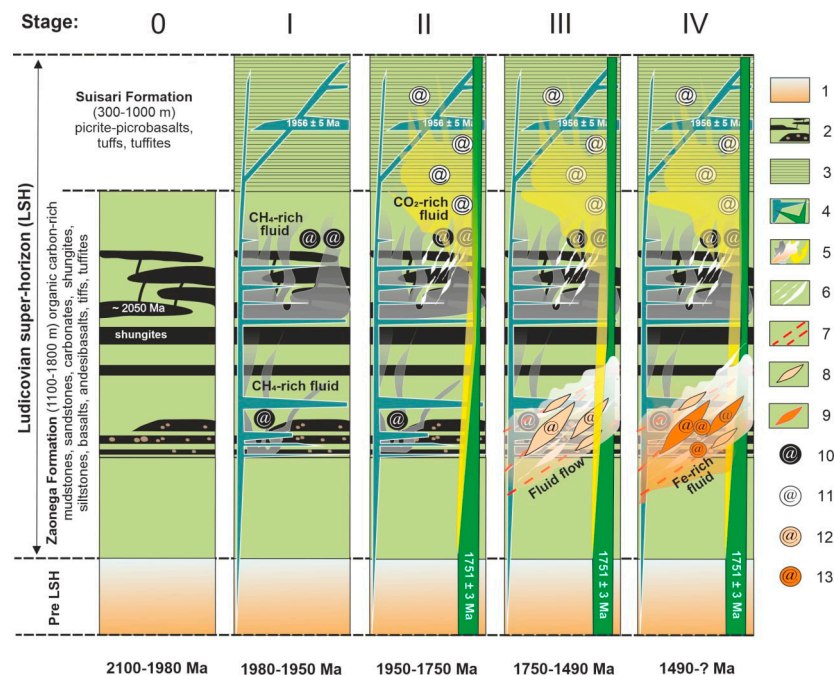


Figure 15. Schematic model of the agate formation stages in the Omega Basin. Compiled using data from [1,2,12–14,16,27,28,30,31,34,91]. Legend: 1—Pre LSH, Paleoproterozoic Jatulian, Sariolian and Sumian super-horizon ca. 2100–2500 Ma, volcanic and sedimentary succession (dolostones, sandstones, conglomerates, basalts, andesitic basalts, tuffs, tuffites); Paleoproterozoic, Ludicovian super-horizon ca. 2100–1920 Ma; 2—organic carbon-rich rocks (shungites), sandstones, siltstones, mudstones, carbonates, basalts, andesibasalts, tuffs, tuffites (Zaonega Formation); 3—picrites, picritic basalts, tuffs, tuffites, tuff-conglomerates, gritstones (Suisari Formation); 4—ca. 1956 and 1751 Ma gabbroids; 5—hydrothermal fluid flows; 6—quartz-carbonate veins systems; 7—tectonic dislocations; 8—Kosmozero/Padma-groups of polymetallic ore veins and stockworks; 9—stockworks subjected to secondary ferruginization; 10—black agates in the ZF volcanics and moss agates in the ZF sediments; 11—lightly colored agates in LSH volcanics; 12—vein agates in stockworks within the ZF sediments; 13—concentrically zoned nodules in the ZF sediments. Stage 0: deposition of organic carbon-rich sedimentary rocks of the ZF and formation of volcanics. Stage I: formation of the volcano-sedimentary sequence of the SF, multiphase intrusions of peridotite and gabbro-dolerite sills, and production of CH₄-rich hydrothermal fluids resulting in the formation of carbon-rich moss agates in the middle part of the ZF and black agates in the upper parts of the ZF. Stage II: intrusion of gabbro-dolerite sills, triggering hydrothermal activity and formation of light-coloured agates in volcanic rocks of the upper part of ZF and lower part of SF. Stage III: formation of regional fold-fault fracture systems within the ZF accompanied by hydrothermal flow resulting in the formation of fine-banded vein agates in the middle part of the ZF. Stage IV: Large-scale, long-term fluid-metasomatic reworking of the volcano-sedimentary rocks within the Omega Basin resulting in the formation of concentrically zoned nodules in the middle part of the ZF.

Stage 0 involves the initial deposition of the ZF, including accumulation of organic carbon-rich sedimentary rocks forming a giant Paleoproterozoic oilfield “Shunga” and appearance of volcanics.

Stage I involves the formation of the volcano-sedimentary sequence of the SF and multi-phase intrusions of peridotite-gabbro-dolerite at 1980–1950 Ma [28]. Magmatic

events triggered the appearance of CH₄-rich hydrothermal fluids, which remobilized the carbonaceous matter from organic carbon-rich sedimentary rocks, resulting in the formation of carbon-rich moss agates in the middle part of the ZF and black agates in the upper parts of the ZF [14].

Stage II involves intrusions of gabbro-dolerite sills at 1780–1750 Ma. This event caused the appearance of local tectonic cracks and CO₂-rich hydrothermal fluid flows, which led to the formation of numerous quartz veins and filling of gas cavities in volcanics. At this stage, lightly colored agates in both the upper part of the ZF and in the lower part of the SF were formed in volcanic rocks [13,14].

Stage III involves the formation of regional fold-fault fracture systems within the ZF at 1750–1490 Ma [12], accompanied by large-scale hydrothermal flow. At this stage, Kosmozero/Padma-groups polymetallic ore veins (Cu-(noble metals)-U-V mineralization) and fine-banded vein agates were formed in the middle part of the ZF.

Stage IV includes circulation of late hydrothermal fluids that resulted in dissolution of carbonate concretions in the organic carbon-rich ZF sedimentary rocks. The fluids were enriched in iron compounds due to interaction with sulfides from organic carbon-rich siltstones and sandstones. Then, cracks and cavities of the concretions were mineralized by Fe-rich silica. Thus, concentrically zoned nodules were formed in the middle part of the ZF. It is possible that the formation of fine-banded agates also occurred at this stage, as indicated by the trace amounts of moganite identified in them, which did not have time to recrystallize into quartz.

The duration of Stage IV is the most controversial. The presence of hydrothermal zircons aged at 1100 to 200 Ma in the ZF volcanic-sedimentary rocks indicates that in the Neoproterozoic-Phanerozoic, the Onega Basin experienced large-scale, long-term fluid-metasomatic reworking [91]. However, the relationship between hydrothermal zircons ages and regional magmatic events is an issue that requires special study. An additional argument for the young age of concentrically zoned nodules is the remarkably high moganite abundance found in them. Moganite is a metastable silica phase and tends to recrystallize into more stable and water-poor granular alpha-quartz during metamorphic alteration [70]. Therefore, nodules exhibiting the elevated moganite content were likely formed significantly earlier compared to fine-banded and moss agates in the organic carbon-rich ZF sedimentary rocks, as well as agates from LSH volcanics.

7. Conclusions

The present contribution provides the first detailed mineralogical investigation of agates occurring in the Paleoproterozoic organic carbon-rich siltstones of the Zaonega Formation (ca. 2050 Ma) within the Onega Basin (Fennoscandian Shield, Russia). The study aimed to highlight the mineralogical features of the agates with a reconstruction of the possible conditions of their formation.

Three main varieties of agates differing in morphology and texture were identified, including concentrically zoned nodules, fine-banded, and carbon-rich moss agates.

The mineral composition of all agate varieties is predominately alpha quartz (micro- and macrocrystalline quartz) with small amounts of hematite and goethite. A distinctive feature of concentrically zoned nodules compared to fine-banded and moss agates is the presence of large amounts of fibrous silica phases (chalcedony and moganite) in addition to crystalline quartz.

Petrographic evidence (Bambauer quartz with growth lines, feathery quartz textures) suggests the participation of low-temperature hydrothermal fluids in agate formation. The presence of accompanying minerals, in particular the sulfides, selenides, carbonates, sulfates, and iron oxides, in agate-bearing veins is also indication of hydrothermal processes.

The mineralogical data show that concentrically zoned nodules could be formed due to the dissolution of carbonate concretions in the organic carbon-rich siltstones and their silicification as a result of hydrothermal processes. The presence of elevated moganite content in the concentrically zoned nodules, together with low Cs and CI values, are

characteristics of immature agates and suggest a relatively young age for the processes that led to their formation compared with fine-banded and moss agates.

Carbonaceous matter in moss agates is present as poorly ordered carbon and is characterized by a low $\delta^{13}\text{C}_{\text{org}}$ value (-25.64%), suggesting a biogenic origin.

The present investigation shows that agates formation in the Onega Basin is a multi-stage process associated with long-term hydrothermal activity.

Agates are characterized by high decorative properties and can be of interest as collectible and ornamental stones. However, the studied agate occurrence does not have gemological-economic significance due to the limited bedrock exposure.

Supplementary Materials: The following supporting information can be downloaded at: <https://www.mdpi.com/article/10.3390/min14050447/s1>, Figure S1: X-ray diffractograms of the host rock and agate samples; Figure S2: DSC, TG, and DTG curves for agate-bearing host rock sample; Table S1: Chemical composition of agate-bearing rock and agates, wt.%; Table S2: Chemical composition of selenium minerals in the agate-bearing veins, EDS microanalysis, wt.%; Table S3: Fitting parameters for the Raman spectra of moganite-rich layers from agate samples in the $400\text{--}550\text{ cm}^{-1}$ range; Table S4: Raman spectral characteristics of carbonaceous matter from moss agates and host rock.

Author Contributions: Conceptualization, data curation, writing, E.N.S. and S.A.S.; field investigation, O.B.L., E.N.S. and S.A.S.; analytical investigation, E.N.S. and O.B.L.; visualization, E.N.S. and S.A.S.; compilation of published geological data, S.A.S. All authors have read and agreed to the published version of the manuscript.

Funding: This research was funded by state assignment to the Institute of Geology, Karelian Research Centre of RAS.

Data Availability Statement: All data are contained within the article and Supplementary Materials.

Acknowledgments: We thank I.S. Inina and S.N. Ivashevskaya (IG KRC RAS, Petrozavodsk, Russia) for their assistance with X-ray diffraction data collection. Our thanks also go to V.L. Andreichev and I.V. Smoleva (IG Komi SC UB RAS, Syktyvkar, Russia) for isotope analysis. We are very grateful to three anonymous reviewers for their comments and advices, which helped to improve the manuscript.

Conflicts of Interest: The authors declare no conflicts of interest.

References

1. Melezhik, V.A.; Medvedev, P.V.; Svetov, S.A. The Onega basin. In *Reading the Archive of Earth's Oxygenation*; Melezhik, V.A., Prave, A.R., Fallick, A.E., Kump, L.R., Strauss, H., Lepland, A., Hanski, E.J., Eds.; Springer: Berlin/Heidelberg, Germany, 2013; pp. 387–490.
2. Puchtel, I.S.; Arndt, N.T.; Hofmann, A.W.; Haase, K.M.; Kröner, A.; Kulikov, V.S.; Kulikova, V.V.; Garbe-Schönberg, C.D.; Nemchin, A.A. Petrology of mafic lavas within the Onega plateau, central Karelia: Evidence for 2.0 Ga plume-related continental crustal growth in the Baltic Shield. *Contrib. Mineral. Petrol.* **1998**, *130*, 134–153. [[CrossRef](#)]
3. Kump, L.R.; Fallick, A.E.; Strauss, H.; Hanski, E.J.; Prave, A.R.; Lepland, A. (Eds.) *Reading the Archive of Earth's Oxygenation. Volume 3: Global Events and the Fennoscandian Arctic Russia—Drilling Early Earth Project*; Springer: Berlin/Heidelberg, Germany, 2013; pp. 1049–1552.
4. Qu, Y.; Lepland, A.; Van Zuilen, M.; Whitehouse, M.; Črne, A.E.; Fallick, A.E. Sample-scale carbon isotopic variability and diverse biomass in the Paleoproterozoic Zaonega Formation, Russia. *Precambrian Res.* **2018**, *315*, 222–231. [[CrossRef](#)]
5. Inostrantsev, A.A. The new end-member of the amorphous carbon series. *Gorn. J.* **1879**, *2*, 314–342. (In Russian)
6. Melezhik, V.A.; Fallick, A.E.; Filippov, M.M.; Larsen, O. Karelian shungite—An indication of 2.0-Ga-old metamorphosed oil-shale and generation of petroleum: Geology, lithology and geochemistry. *Earth Sci. Rev.* **1999**, *47*, 1–40. [[CrossRef](#)]
7. Prave, A.R.; Kirsimäe, K.; Lepland, A.; Fallick, A.E.; Kreitsmann, T.; Deines, Y.E.; Romashkin, A.E.; Rychanchik, D.V.; Medvedev, P.V.; Moussavou, M.; et al. The grandest of them all: The Lomagundi–Jatuli Event and Earth's oxy-genation. *J. Geol. Soc.* **2022**, *179*, jgs2021-036. [[CrossRef](#)]
8. Chistyakov, A.V.; Sharkov, E.V.; Grokhovskaya, T.L.; Bogatnikov, O.A.; Muravitskaya, G.N.; Grinevich, N.G. Petrology of the Europe-Largest Burakovka early Paleoproterozoic layered pluton (Southern Karelia, Russia). *Russ. J. Earth Sci.* **2002**, *4*, 35–75. [[CrossRef](#)]
9. Golubev, A.I.; Ivashchenko, V.I.; Trofimov, N.N.; Lavrov, M.M. Complex metalliferous useful mineral deposits. In *Paleoproterozoic Onega Structure: Geology, Tectonics, Structure, and Metallogeny*; Glushanin, L.V., Sharov, N.V., Shchiptsov, V.V., Eds.; Karelian Research Centre, RAS: Petrozavodsk, Russia, 2011; pp. 385–396. (In Russian)
10. Trofimov, N.N.; Golubev, A.I. Geodynamic conditions of formation and metallogeny of the Onega depression. *Ores Met.* **2000**, *5*, 10–25. (In Russian)

11. Borozdin, A.P.; Polekhovskii, Y.S.; Glebovitskii, V.A.; Bushmin, S.A.; Belyatskii, B.V.; Savva, E.V. Age of metasomatism and ore formation in the Srednyaya Padma vanadium-precious metals-uranium deposit (Karelia, Baltic shield). *Doklady Earth Sci.* **2014**, *454*, 68–71. [[CrossRef](#)]
12. Kuleshevich, L.V.; Lavrov, O.B. Mineral–geochemical features of Paleoproterozoic gold–copper–sulfide, noble metal–copper–uranium, and noble–metal–copper–uranium–vanadium deposits and ore occurrences of Karelia. *Geol. Ore Depos.* **2022**, *64*, 123–143. [[CrossRef](#)]
13. Svetova, E.N.; Svetov, S.A. Mineralogy and geochemistry of agates from Paleoproterozoic volcanic rocks of the Karelian Craton, Southeast Fennoscandia (Russia). *Minerals* **2020**, *10*, 1106. [[CrossRef](#)]
14. Svetova, E.N.; Chazhengina, S.Y.; Stepanova, A.V.; Svetov, S.A. Black agates from Paleoproterozoic pillow lavas (Onega Basin, Karelian Craton, NW Russia): Mineralogy and proposed origin. *Minerals* **2021**, *11*, 918. [[CrossRef](#)]
15. Arestova, N.A.; Chekulaev, V.P.; Lobach-Zhuchenko, S.B.; Kucherovskii, G.A. Formation of the Archean crust of the ancient Vodlozero domain (Baltic shield). *Stratigr. Geol. Correl.* **2015**, *23*, 119–130. [[CrossRef](#)]
16. Kulikov, V.S.; Svetov, S.A.; Slabunov, A.I.; Kulikova, V.V.; Polin, A.K.; Golubev, A.I.; Gorkovets, V.Y.; Ivashchenko, V.I.; Gogolev, M.A. Geological map of Southeastern Fennoscandia (scale 1:750,000): A new approach to map compilation. *Trans. KarRC RAS* **2017**, *2*, 3–41. [[CrossRef](#)]
17. Slabunov, A.I.; Lobach-Zhuchenko, S.B.; Bibikova, E.V.; Sorjonen-Ward, P.; Balagansky, V.V.; Volodichev, O.I.; Shchipansky, A.A.; Svetov, S.A.; Chekulaev, V.P.; Arestova, N.A.; et al. The Archean nucleus of the Fennoscandian (Baltic) Shield. In *European Lithosphere Dynamics*; Gee, D.G., Stephenson, R.A., Eds.; Memoirs, Geological Society: London, UK, 2006; Volume 32, pp. 627–644.
18. Hölttä, P.; Heilimo, E.; Huhma, H.; Kontinen, A.; Lauri, L.; Slabunov, A. Paleoproterozoic Rocks in the Fennoscandian Shield. In *Earth's Oldest Rocks*, 2nd ed.; Kranendonk, M.J.V., Bennett, V.C., Hoffmann, J.E., Eds.; Elsevier: Amsterdam, The Netherlands, 2019; Chapter 32; pp. 819–835.
19. Galdobina, L.P. The Ludicovian Super-horizon. In *Geology of Karelia*; Sokolov, V.A., Ed.; Nauka: Leningrad, Russia, 1987; pp. 59–67. (In Russian)
20. Buseck, P.R.; Galdobina, L.P.; Kovalevski, V.V.; Rozkova, N.N.; Valley, J.W.; Zaidenberg, A.Z. Shungites: The C-rich rocks of Karelia, Russia. *Can. Mineral.* **1997**, *35*, 1363–1378.
21. Kump, L.R.; Junium, C.; Arthur, M.A.; Brasier, A.; Fallick, A.; Melezhik, V.; Lepland, A.; Črne, A.E.; Luo, G.M. Isotopic evidence for massive oxidation of organic matter following the great oxidation event. *Science* **2011**, *334*, 1694–1696. [[CrossRef](#)]
22. Filippov, M.M. *Shungite Rocks of the Onega Structure*; Karelian Science Centre, RAS: Petrozavodsk, Russia, 2002; 282p. (In Russian)
23. Krupenik, V.A.; Akhmedov, A.M.; Sveshnikova, K.Y. Structure of the Onega sequence based on Onega parametric borehole. In *Paleoproterozoic Onega Structure: Geology, Tectonics, Structure, and Metallogeny*; Glushanin, L.V., Sharov, N.V., Shchiptsov, V.V., Eds.; Karelian Research Centre, RAS: Petrozavodsk, Russia, 2011; pp. 171–176. (In Russian)
24. Filippov, M.M.; Golubev, A.I. Carbon isotope composition of shungite rocks. In *The Organic Matter of Karelian Shungite Rocks (Genesis, Evolution and the Methods of Study)*; Filippov, M.M., Ed.; Karelian Science Centre, RAS: Petrozavodsk, Russia, 1994; pp. 32–43. (In Russian)
25. Melezhik, V.A.; Fallick, A.E.; Filippov, M.M.; Lepland, A.; Rychanchik, D.V.; Deines, Y.E.; Medvedev, P.V.; Romashkin, A.E.; Strauss, H. Petroleum surface oil seeps from a Paleoproterozoic petrified giant oilfield. *Terra Nova* **2009**, *21*, 119–126. [[CrossRef](#)]
26. Chazhengina, S.Y.; Stepanova, A.V.; Ustinova, V.V.; Svetov, S.A. Amorphous carbonaceous material in Paleoproterozoic pillow lavas (Onega Basin, NW Russia): Origin, source and migration. *Lithos* **2023**, *460*, 107373. [[CrossRef](#)]
27. Hannah, J.L.; Stein, H.J.; Yang, G.; Zimmerman, A.; Melezhik, V.A.; Filippov, M.M.; Turgeon, S.C. Re–Os geochronology of a 2.05 Ga fossil oil field near Shunga, Karelia, NW Russia. In Proceedings of the Abstracts of the 33 International Geological Congress, Oslo, Norway, 5–14 August 2008.
28. Stepanova, A.V.; Samsonov, A.V.; Larionov, A.N. The final episode of the middle proterozoic magmatism in the Onega structure: Data on Trans-Onega dolerites. *Trans. KarRC RAS* **2014**, *1*, 3–16.
29. Martin, A.P.; Prave, A.R.; Condon, D.J.; Lepland, A.; Fallick, A.E.; Romashkin, A.E.; Medvedev, P.V.; Rychanchik, D.V. Multiple Palaeoproterozoic carbon burial episodes and excursions. *Earth Planet. Sci. Lett.* **2015**, *424*, 226–236. [[CrossRef](#)]
30. Kulikov, V.S.; Rychanchik, D.V.; Golubev, A.I.; Filippov, M.M.; Tarkhanov, G.V.; Frik, M.G.; Svetov, S.A.; Kulikova, V.V.; Sokolov, S.Y.; Romashkin, A.E. Stratigraphy and magmatism. Ludicovian. In *Paleoproterozoic Onega Structure: Geology, Tectonics, Structure, and Metallogeny*; Glushanin, L.V., Sharov, N.V., Shchiptsov, V.V., Eds.; Karelian Research Centre, RAS: Petrozavodsk, Russia, 2011; pp. 67–101. (In Russian)
31. Leonov, M.G.; Kulikov, V.S.; Zykov, D.S.; Kolodyazhny, S.Y.; Poleshchuk, A.V. Tectonics. In *Paleoproterozoic Onega Structure: Geology, Tectonics, Structure, and Metallogeny*; Glushanin, L.V., Sharov, N.V., Shchiptsov, V.V., Eds.; Karelian Research Centre, RAS: Petrozavodsk, Russia, 2011; pp. 127–170. (In Russian)
32. Spiridonov, E.M.; Putintzeva, E.V.; Lavrov, O.B.; Ladygin, V.M. Kronstedtite, pumpelliite, prehnite and lenilenapeite in the metaagates and metabasalts of the early Proterozoic trap formation in the northern Onega region. In Proceedings of the Conference Lomonosov Readings, Moscow, Russia, 17–27 April 2017; Moscow State University: Moscow, Russia, 2017. Available online: https://conf.msu.ru/file/event/4305/eid4305_attach_b0acc3e7de2cd859225469534617a6272d70ce50.pdf (accessed on 21 February 2024). (In Russian)
33. Filipov, M.M.; Deynes, Y.E. *Subtabular Type of Shungite Deposits of Karelia*; KarSC RAS: Petrozavodsk, Russia, 2018; 261p. (In Russian)

34. Glebovitskii, V.A.; Bushmin, S.A.; Belyatsky, B.V.; Bogomolov, E.S.; Borozdin, A.P.; Savva, E.V.; Lebedeva, Y.M. RB-SR age of metasomatism and ore formation in the low-temperature shear zones of the Fenno-Karelian Craton, Baltic Shield. *Petrology* **2014**, *22*, 184–204. [[CrossRef](#)]
35. Lavrov, O.B.; Kuleshevich, L.V. Mineral associations of low-temperature veins oxidized zones of the Kondoberezhskaja occurrence (Onezhskaja srtructure, Karelia). In Proceedings of the Fersman Scientific Session of the GI KSC RAS, Apatity, Russia, 5–8 April 2020; Volume 17, pp. 317–321. (In Russian) [[CrossRef](#)]
36. Götze, J.; Nasdala, L.; Kleeberg, R.; Wenzel, M. Occurrence and distribution of “moganite” in agate/chalcedony: A combined micro-Raman, Rietveld, and cathodoluminescence study. *Contrib. Mineral. Petrol.* **1998**, *133*, 96–105. [[CrossRef](#)]
37. Kouketsu, Y.; Mizukami, T.; Mori, H.; Endo, S.; Aoya, M.; Hara, H.; Nakamura, D.; Wallis, S. A new approach to develop the Raman carbonaceous material geothermometer for low-grade metamorphism using peak width. *Isl. Arc.* **2014**, *23*, 33–50. [[CrossRef](#)]
38. Behera, D.; Nandi, B.K.; Bhattacharya, S. Chemical properties and combustion behavior of constituent relative density fraction of a thermal coal. *Energy Sources Part A Recovery Util. Environ. Eff.* **2019**, *41*, 654–664. [[CrossRef](#)]
39. Wada, H.; Tomita, T.; Matsuura, K.; Iuchi, K.; Ito, M.; Morikiyo, T. Graphitization of carbonaceous matter during metamorphism with references to carbonate and pelitic rocks of contact and regional metamorphisms, Japan. *Contrib. Mineral. Petrol.* **1994**, *118*, 217–228. [[CrossRef](#)]
40. Dong, G.; Morrison, G.; Jaireth, S. Quartz textures in epithermal veins, Queensland—Classification, origin, and implication. *Econ. Geol.* **1995**, *90*, 1841–1856. [[CrossRef](#)]
41. Bambauer, H.U.; Brunner, G.O.; Laves, F. Beobachtungen über Lamellenbau an Bergkristallen1. *Z. Kristallogr* **1961**, *116*, 173–181. (In German) [[CrossRef](#)]
42. Murata, J.; Norman, M.B. An index of crystallinity for quartz. *Am. J. Sci.* **1976**, *276*, 1120–1130. [[CrossRef](#)]
43. Kuznetsov, S.K.; Svetova, E.N.; Shanina, S.N.; Filippov, V.N. Minor Elements in Quartz from Hydrothermal-Metamorphic Veins in the Nether Polar Ural Province. *Geochemistry* **2012**, *50*, 911–925. [[CrossRef](#)]
44. Ferrari, A.C.; Robertson, J. Interpretation of Raman spectra of disordered and amorphous carbon. *Phys. Rev.* **2000**, *61*, 14095–14107. [[CrossRef](#)]
45. Wopenka, B.; Pasteris, J.D. Structural characterization of kerogens to granulite-facies graphite: Applicability of Raman microprobe spectroscopy. *Am. Mineral.* **1993**, *78*, 533–557.
46. Kholodkevich, S.V.; Berezkin, V.I.; Davydov, V.Y. Specific structural features and thermal resistance of shungite carbon to graphitization. *Phys. Solid State* **1999**, *41*, 1291–1294. [[CrossRef](#)]
47. Jehlicka, J.; Urban, O.; Pokorný, J. Raman spectroscopy of carbon and solid bitumens in sedimentary and metamorphic rocks. *Spectrochim. Acta* **2003**, *59*, 2341–2352. [[CrossRef](#)] [[PubMed](#)]
48. Van Zuilen, M.A.; Fliegel, D.; Wirth, R.; Lepland, A.; Qu, Y.; Schreiber, A.; Romashkin, A.E.; Philippot, P. Mineral-templated growth of natural graphite films. *Geochim. Cosmochim. Acta* **2012**, *83*, 252–262. [[CrossRef](#)]
49. Beyssac, O.; Goffé, B.; Chopin, C.; Rouzaud, J.N. Raman spectra of carbonaceous material in metasediments: A new geothermometer. *J. Metamorph. Geol.* **2002**, *20*, 859–871. [[CrossRef](#)]
50. Buseck, P.R.; Beyssac, O. From Organic Matter to Graphite: Graphitization. *Elements* **2014**, *10*, 421–426. [[CrossRef](#)]
51. De Faria, D.L.A.; Venâncio, S.S.; de Oliveira, M.T. Raman microspectroscopy of some iron oxides and oxyhydroxides. *J. Raman Spectrosc.* **1997**, *28*, 873–878. [[CrossRef](#)]
52. Das, S.; Hendry, M.J. Application of Raman spectroscopy to identify iron minerals commonly found in mine wastes. *Chem. Geol.* **2011**, *290*, 101–108. [[CrossRef](#)]
53. Krolop, P.; Jantschke, A.; Gilbricht, S.; Niiranen, K.; Seifert, T. Mineralogical Imaging for Characterization of the Per Geijer Apatite Iron Ores in the Kiruna District, Northern Sweden: A Comparative Study of Mineral Liberation Analysis and Raman Imaging. *Minerals* **2019**, *9*, 544. [[CrossRef](#)]
54. Van Tuyl, F.M. The stratigraphy of the Mississippian formations of Iowa: Iowa Geol. Survey. *Ann. Rep.* **1922**, *30*, 33–349.
55. Hayes, J.B. Geodes and concretions from the Mississippian Warsaw Formation. Keokuk region, Iowa, Illinois, Missouri. *Sediment. Petrol.* **1964**, *34*, 123–133.
56. Chown, T.M.; Elkins, J.E. The origin of quartz geodes and cauliflower cherts through the silification of anhydrite nodules. *J. Sediment. Petrol.* **1974**, *44*, 885–903.
57. Godovikov, A.A.; Ripinen, O.I.; Motorin, S.G. *Agates*; Nedra: Moscow, Russia, 1987; 368p. (In Russian)
58. Götze, J.; Möckel, R.; Pan, Y. Mineralogy, Geochemistry and Genesis of Agate—A Review. *Minerals* **2020**, *10*, 1037. [[CrossRef](#)]
59. Powolny, T.; Dumańska-Słowik, M.; Sikorska-Jaworowska, M.; Wójcik-Baniaaet, M. Agate mineralization in spilitized Permian volcanics from “Borówno” quarry (Lower Silesia, Poland)—Microtextural, mineralogical, and geochemical constraints. *J. Ore Geol. Rev.* **2019**, *114*, 103–130. [[CrossRef](#)]
60. Pršek, J.; Dumańska-Słowik, M.; Powolny, T.; Natkaniec-Nowak, L.; Tobała, T.; Zych, D.; Skrepnicka, D. Agates from Western Atlas (Morocco)—Constraints from mineralogical and microtextural characteristics. *Minerals* **2020**, *10*, 198. [[CrossRef](#)]
61. Svetova, E.N.; Palyanova, G.A.; Borovikov, A.A.; Posokhov, V.F.; Moroz, T.N. Mineralogy of Agates with Amethyst from the Tevinskoye Deposit (Northern Kamchatka, Russia). *Minerals* **2023**, *13*, 1051. [[CrossRef](#)]
62. Sander, M.V.; Black, J.E. Crystallization and recrystallization of growth-zoned vein quartz crystals from epithermal systems; implications for fluid inclusion studies. *Econ. Geol.* **1988**, *83*, 1052–1060. [[CrossRef](#)]

63. Marinova, I.; Ganey, V.; Titorenkova, R. Colloidal origin of colloform-banded textures in the Paleogene low-sulfidation Khan Krum gold deposit, SE Bulgaria. *Miner. Depos.* **2014**, *49*, 49–74. [[CrossRef](#)]
64. Yilmaz, T.I.; Duschl, F.; Di Genova, D. Feathery and network-like filamentous textures as indicators for the re-crystallization of quartz from a metastable silica precursor at the Rusey Fault Zone, Cornwall, UK. *Solid Earth* **2016**, *7*, 1509–1519. [[CrossRef](#)]
65. Moxon, T.; Rios, S. Moganite and water content as a function of age in agate: An XRD and thermogravimetric study. *Eur. J. Mineral.* **2004**, *4*, 693–706. [[CrossRef](#)]
66. Moxon, T.; Palyanova, G. Agate Genesis: A Continuing Enigma. *Minerals* **2020**, *10*, 953. [[CrossRef](#)]
67. Zhang, X.; Ji, L.; He, X. Gemological characteristics and origin of the Zhanguohong agate from Beipiao, Liaoning province, China: A combined microscopic, X-ray diffraction, and Raman spectroscopic study. *Minerals* **2020**, *10*, 401. [[CrossRef](#)]
68. Götze, J.; Stanek, K.; Orozco, G.; Liesegang, M.; Mohr-Westheide, T. Occurrence and Distribution of Moganite and Opal-CT in Agates from Paleocene/Eocene Tuffs, El Picado (Cuba). *Minerals* **2021**, *11*, 531. [[CrossRef](#)]
69. Conte, A.; Della Ventura, G.; Rondeau, B.; Romani, M.; Guidi, M.C.; La, C.; Napoleoni, C.; Lucci, F. Hydrothermal genesis and growth of the banded agates from the Allumiere-Tolfa volcanic district (Latium, Italy). *Phys. Chem. Miner.* **2022**, *49*, 39. [[CrossRef](#)]
70. Moxon, T.; Reed, S.J.B.; Zhang, M. Metamorphic effects on agate found near the Shap granite, Cumbria: As demonstrated by petrography, X-ray diffraction spectroscopic methods. *Miner. Mag.* **2007**, *71*, 461–476. [[CrossRef](#)]
71. Moxon, T.; Carpenter, M.A. Crystallite growth kinetics in nanocrystalline quartz (agate and chalcedony). *Miner. Mag.* **2009**, *73*, 551–568. [[CrossRef](#)]
72. Moxon, T.; Nelson, D.R.; Zhang, M. Agate recrystallization: Evidence from samples found in Archaean and Proterozoic host rocks, Western Australia. *Aust. J. Earth Sci.* **2006**, *53*, 235–248. [[CrossRef](#)]
73. Svetova, E.N.; Svetov, S.A. Agates from Mesoproterozoic Volcanics (Pasha–Ladoga Basin, NW Russia): Characteristics and Proposed Origin. *Minerals* **2023**, *13*, 62. [[CrossRef](#)]
74. Moxon, T. Agates: A study of ageing. *Eur. J. Mineral.* **2002**, *14*, 1109–1118. [[CrossRef](#)]
75. Joosu, L.; Lepland, A.; Kirsimäe, K.; Romashkin, A.E.; Roberts, N.M.W.; Martin, A.P.; Črne, A.E. The REE-composition and petrography of apatite in 2 Ga Zaonega Formation, Russia: The environmental setting for phosphogenesis. *Chem. Geol.* **2015**, *395*, 88–107. [[CrossRef](#)]
76. Dumańska-Słowik, M.; Natkaniec-Nowak, L.; Kotarba, M.J.; Sikorska, M.; Rzymelka, J.A.; Łoboda, A.; Gawęł, A. Mineralogical and geochemical characterization of the “bituminous” agates from Nowy Kościół (Lower Silesia). *J. Mineral. Geochem.* **2008**, *184*, 255–268. [[CrossRef](#)]
77. Natkaniec-Nowak, L.; Dumańska-Słowik, M.; Pršek, J.; Lankosz, M.; Wróbel, P.; Gawęł, A.; Kowalczyk, J.; Kocemba, J. Agates from Kerrouchen (The Atlas Mountains, Morocco): Textural Types and Their Gemmological Characteristics. *Minerals* **2016**, *6*, 77. [[CrossRef](#)]
78. Götze, J.; Nasdala, L.; Kempe, U.; Libowitzky, E.; Rericha, A.; Vennemann, T. The origin of black colouration in onyx agate from Mali. *Miner. Mag.* **2012**, *76*, 115–127. [[CrossRef](#)]
79. Chazhengina, S.Y.; Kovakevski, V.V. Raman spectroscopy of weathered shungites. *J. Raman Spectrosc.* **2017**, *48*, 1590–1596. [[CrossRef](#)]
80. Deines, P. The carbon isotope geochemistry of mantle xenoliths. *Earth Sci. Rev.* **2002**, *58*, 247–278. [[CrossRef](#)]
81. Schwab, V.; Spangenberg, J.E.; Grimalt, J.O. Chemical and carbon isotopic evolution of hydrocarbons during prograde metamorphism from 100 °C to 550 °C: Case study in the Liassic black shale formation of Central Swiss Alps. *Geochim. Cosmochim. Acta* **2005**, *69*, 1825–1840. [[CrossRef](#)]
82. Maliva, R.G. Quartz geodes: Early diagenetic silicified anhydrite nodules related to dolomitization. *J. Sed. Res.* **1987**, *57*, 1054–1059.
83. Götze, J.; Möckel, R.; Kempe, U.; Kapitonov, I.; Vennemann, T. Origin and characteristics of agates in sedimentary rocks from the Dryhead area, Montana/USA. *Mineral. Mag.* **2009**, *73*, 673–690.
84. Tripp, R.B. The mineralogy of Warsaw Formation geodes. *Iowa Acad. Sci. Proc.* **1959**, *66*, 350–356.
85. Clark, R. *Fairburn Agate Gem of South Dakota*; Silverwind Agates: Appleton, WI, USA, 2002; 104p.
86. Tucker, M.E. Quartz replaced anhydrite nodules (“Bristol diamonds”) from the Triassic of the Bristol District. *Geol. Mag.* **1976**, *113*, 569–574. [[CrossRef](#)]
87. Gómez-Alday, J.J.; García-Garmilla, F.; Elorza, J. Origin of quartz geodes from Laño and Tubilla del Agua sections (middle–upper Campanian, Basque-Cantabrian Basin, northern Spain): Isotopic differences during diagenetic processes. *Geol. J.* **2002**, *37*, 117–134. [[CrossRef](#)]
88. Sletov, V.A. On the ontogeny of silica geodes from coal formation of the Moscow region. In *Essays on Genetic Mineralogy, Collection of Articles*; “Science”: Moscow, Russia, 1976. Available online: <http://geo.web.ru/mindraw/bibl10.htm> (accessed on 27 February 2024). (In Russian)
89. Palyanova, G.; Sidorov, E.; Borovikov, A.; Seryotkin, Y. Copper-Containing Agates of the Avacha Bay (Eastern Kamchatka, Russia). *Minerals* **2020**, *10*, 1124. [[CrossRef](#)]

90. Shen, M.; Lu, Z.; He, X. Mineralogical and Geochemical Characteristics of Banded Agates from Placer Deposits: Implications for Agate Genesis. *ACS Omega* **2022**, *7*, 23858–23864. [[CrossRef](#)] [[PubMed](#)]
91. Goltsin, N.A.; Lokhov, K.I.; Kapitonov, I.N.; Polekhovskiy, Y.S.; Lobikov, A.F.; Sergeev, S.A. Polystage transformations of carbon rich rocks of the ludicovian of the Onega Basin. *Reg. Geol. Metallog.* **2010**, *41*, 61–74. (In Russian)

Disclaimer/Publisher’s Note: The statements, opinions and data contained in all publications are solely those of the individual author(s) and contributor(s) and not of MDPI and/or the editor(s). MDPI and/or the editor(s) disclaim responsibility for any injury to people or property resulting from any ideas, methods, instructions or products referred to in the content.